Physics   Faculty Publications & Research

2007

Relativistic Jets in the Radio Reference Frame Image Database. I. Apparent Speeds from the First 5 Years of Data

B. G. Piner
Whittier College, gpiner@whittier.edu

M. Mahmud

A. L. Fey

K. Gospodinova

Follow this and additional works at: https://poetcommons.whittier.edu/phys

RELATIVISTIC JETS IN THE RADIO REFERENCE FRAME IMAGE DATABASE. I. APPARENT SPEEDS FROM THE FIRST 5 YEARS OF DATA

B. G. PINER,[1,2] M. MAHMUD,[1,3] A. L. FEY,[4] AND K. GOSPODINOVA[1]

ABSTRACT

We present the results of an analysis of relativistic jet apparent speeds from VLBI images in the Radio Reference Frame Image Database (RRFID). The images are snapshot VLBI images at 8 and 2 GHz using the VLBA, plus up to 10 additional antennas that provide global VLBI coverage. We have analyzed the 8 GHz images from the first 5 years of the database (1994–1998), for all sources observed at three or more epochs during this time range. This subset comprises 966 images of 87 sources. The sources in this subset have an average of 11 epochs of observation over the years 1994–1998, with the best-observed sources having 19 epochs. About half of the sources in this RRFID kinematic survey have not been previously studied with multiepoch VLBI observations. We have measured apparent speeds for a total of 184 jet components in 77 sources, of which the best-measured 94 component speeds in 54 sources are used in the final analysis. The apparent speed distribution shows a peak at low apparent speeds (consistent with stationary components), a tail extending out to apparent speeds of about $30c$, and a mean apparent speed of $3.6c$. A total of 36 of the sources in this paper are also included in the 2 cm VLBA survey by Kellermann et al., with similar angular resolution, sensitivity, and time range. For those sources, we present a detailed component-by-component comparison of the apparent speeds measured by the 2 cm survey and those measured in this paper. Many of the independent apparent speed measurements agree very well, but for approximately 25% of the components we find significant differences in the apparent speeds measured by the two surveys. The leading cause of these discrepancies is differences in how the two surveys have identified jet components from epoch to epoch.

Key words: galaxies: active — galaxies: jets — radio continuum: galaxies

Online material: machine-readable tables

1. INTRODUCTION

Among the most remarkable discoveries made during the early days of the VLBI technique was the apparent superluminal motion exhibited by the jets of some extragalactic radio sources (e.g., Whitney et al. 1971; Cohen et al. 1971), which can be explained as a relativistic jet moving nearly along the line of sight (e.g., Blandford & Königl 1979). Multiepoch studies of various individual sources began soon after the discovery of this phenomenon, with different research groups taking the responsibility for monitoring different sources with ad hoc VLBI arrays. However, the need was soon recognized for multiepoch surveys of many sources so that the apparent speeds of relativistic jets could be studied in a uniform manner, both to learn about the jets themselves and to use in applications ranging from unified models of AGNs to cosmology. Early efforts to assemble multiepoch data for many sources relied on collecting single-source results from the literature (e.g., Vermeulen & Cohen 1994), but such assemblages can be biased because they include only the data that observers have elected to publish. Observing and reducing multiple epochs of VLBI data on many sources is a time-consuming task that became manageable with the advent of dedicated VLBI arrays such as the National Radio Astronomy Observatory's Very Long Baseline Array (VLBA) and the European VLBI Network (EVN), and the past few years have seen publication of results from two large multiepoch VLBI surveys (here "large" is defined as exceeding about 500 images in the survey), which we summarize below.

The Caltech–Jodrell Bank flat-spectrum (CJF) survey is a complete flux-limited sample of 293 flat-spectrum radio sources, drawn from the 6 and 20 cm Green Bank surveys. The CJF survey has obtained 3–5 epochs of VLBI data at 5 GHz spanning 4–8 yr on each of these 293 sources, over the years 1990–2000 (Vermeulen et al. 2003), with a typical separation between observations of about 2 yr (Britzen et al. 1999). Some results on the measured apparent speeds, including statistics derived from 597 component speed measurements in 262 sources, are given by Vermeulen et al. (2003).

The 2 cm survey (Kellermann et al. 1998, 2004; Zensus et al. 2002; Kovalev et al. 2005) observed a smaller number of sources than the CJF survey, but at a higher angular resolution because the observations were at a higher frequency of 15 GHz (wavelength of 2 cm). This survey consisted of multiepoch observations with the VLBA of over 100 sources between the years 1994 and 2001. The jet kinematics derived from these observations are presented by Kellermann et al. (2004, hereafter K04). That paper presented apparent speeds for 208 jet features in 110 sources, measured from an average of six epochs per source over the years 1994–2001, yielding a typical epoch spacing for each source of about one observation per year. Since 2001, the 2 cm survey has continued as the MOJAVE survey, with polarization observations added, and with a somewhat altered source list to ensure a statistically complete sample. First-epoch results from the MOJAVE survey were presented by Lister & Homan (2005; linear polarization measurements) and Homan & Lister (2006; circular polarization measurements).

In this paper, we present results from a new multiepoch VLBI kinematic survey, drawn from the US Naval Observatory's Radio

---

[1] Department of Physics and Astronomy, Whittier College, Whittier, CA 90608, USA; gpiner@whittier.edu.

[2] Jet Propulsion Laboratory, California Institute of Technology, Pasadena, CA 91109, USA.

[3] Department of Physics, University College Cork, Cork, Ireland.

[4] US Naval Observatory, Washington, DC 20392, USA; afey@usno.navy.mil.

Reference Frame Image Database (RRFID).[5] The RRFID is the result of an ongoing program to image radio reference frame sources on a regular basis. The goal is to establish a database of images of all radio reference frame sources at the same wavelengths as those used for precise astrometry. The multiepoch VLBI data allow the monitoring of sources for variability or structural changes so that they can be evaluated for continued suitability as radio reference frame objects. RRFID observations are performed with the full 10 station VLBA, with the addition of up to 10 geodetic VLBI antennas for global VLBI coverage. Observations are performed simultaneously at frequencies of 8 and 2 GHz. Observations began in 1994 and have continued through the present; however, the RRFID image database is currently well filled only through the end of 1998, covering the first 5 years of observations. At this writing, the database contains 4164 images of 517 sources. Imaging results from this database have been presented by Fey et al. (1996) and Fey & Charlot (1997, 2000). The RRFID has also recently begun to include multiepoch VLBA observations at higher frequencies of 24 and 43 GHz (K and Q band).[6]

The RRFID is not a flux-limited sample, and membership in the database is limited to those sources useful for astrometry or geodesy. Sources selected for astrometry and geodesy have historically been the brightest known compact sources. The source list has evolved over time as the arrays used evolved and included longer baselines and became more sensitive, thus rejecting sources previously considered compact in favor of weaker, more core-dominated sources that are known to produce consistent geodetic results. There has also been an attempt to select sources as uniformly distributed on the sky as possible; this can only be carried so far, but it gets easier as the sensitivity to weaker sources increases. The final result is that while the RRFID contains many observations of well-known sources (for example, BL Lac), there are other well-known sources (for example, 3C 273) that are not well represented in the database. On the other hand, some strong sources that may have been only sparsely observed by the astronomical community have very good coverage in the RRFID. Because of this historical evolution of the source list, the exact nature of the biases that this lack of predefined selection criteria may introduce into statistical quantities calculated from the RRFID is not known.

This paper presents the results of a VLBI kinematic survey (hereafter the RRFID kinematic survey), selected as a subset of the currently available observations in the RRFID. For this paper, we have selected 8 GHz observations of all sources observed at three or more epochs between the beginning of the database in 1994 July through the last, nearly contiguous epoch in the database in 1998 December; this subset covers 19 astrometric VLBA experiments. These selection criteria yield a total of 87 sources, with a total of 966 8 GHz images. For these 87 sources, there are then an average of 11 epochs per source over this 5 yr timespan, with the best-observed sources being observed at all 19 epochs. This survey thus covers a slightly smaller number of sources than the 2 cm survey, but with about twice the average number of epochs per source. The epoch spacing in the RRFID is not evenly distributed—there are six astrometric VLBA experiments from the 3 years 1994–1996 (yielding an average epoch spacing of about 0.5 yr for sources observed at all epochs), and 13 astrometric VLBA experiments from the 2 years 1997–1998 (yielding an average epoch spacing of about 2 months for sources observed at all epochs). Astrometric VLBA experiments (the RDV series) have continued to use an epoch spacing of about 2 months since 1998.

This survey thus explores the jet kinematics using a much smaller average epoch spacing than has been used in previous large VLBI surveys, and this is potentially quite important (Jorstad et al. [2001] and Homan et al. [2001] used similarly short time spacing, but for smaller numbers of sources). A persistent problem in the interpretation of multiepoch VLBI images is in the identification of jet "components" from epoch to epoch across the series of images; this is arguably the most subjective step in the usual process of measuring jet apparent speeds. A subset of sources may exhibit clear motions of bright well-separated features, but in other sources there can be ambiguities in the identification of features that can be influenced by the epoch spacing of the observations. (In particular, a "strobing" effect can cause a larger number of rapidly moving features to be interpreted as a smaller number of slower moving features.) This general problem of component identifications is discussed in the context of the CJF survey by Vermeulen et al. (2003). About half of the sources included in this paper are also included in the 2 cm survey (many of the other half have not been previously observed with multiepoch VLBI), and for those sources that are common to both surveys we are able to perform a detailed comparison of our apparent speed measurements with those of K04 over the same time range, in order to determine if different epoch spacings influence the measurement of jet speeds. This is the first time known to us that such a large comparison of kinematic results for the same sources from different VLBI surveys has been attempted, and such a comparison is important for assessing the repeatability of apparent speed measurements.

We note that the application of geodetic or astrometric VLBI data to astrophysics is not new; see, for example, the study of geodetic VLBI observations of EGRET blazars by Piner & Kingham (1997a, 1997b, 1998). What is different about this application of geodetic VLBI data is that now the data are drawn from observations with the VLBA that have been designed for accurate imaging of the source structure, so that the images are of much higher quality than the images in those earlier papers that relied solely on data from dedicated geodetic antennas.

In this paper we present only the jet apparent speeds from the first 5 years of 8 GHz data in the RRFID. Future papers in this series will study other aspects of jet astrophysics from both the 8 and 2 GHz data in the RRFID, such as correlations of the jet apparent speeds with other source properties, bending of the parsec-scale jets and their misalignment with kiloparsec-scale structures, transverse structures (or lack thereof) in the parsec-scale jets, and measurements of jet apparent speeds using an expanded time baseline of data (once observations from the years after 1998 are added to the RRFID).

The structure of this paper is as follows: in § 2 we describe the RRFID observations in detail; in § 3 we describe the procedures used in calibrating, imaging, and model-fitting the data; in § 4 we present the kinematic results; and in § 5 we compare those kinematic results to those obtained by the 2 cm survey (K04) for the common sources. Throughout this paper we assume cosmological parameters $H_0 = 71$ km s^{-1} Mpc^{-1}, $\Omega_m = 0.27$, and $\Omega_\Lambda = 0.73$. When results from other papers are quoted, they have been converted to this cosmology.

2. OBSERVATIONS

Observations were made using the 10 antennas of the VLBA (Napier et al. 1994) of the National Radio Astronomy Observatory (NRAO),[7] along with an array consisting of up to

TABLE 1
OBSERVATION LOG

Epoch	VLBA Observation Code	Antennas	Reference
1994 Jul 8	BR005	VLBA	1
1995 Apr 12...........................	BR025	VLBA	2
1995 Jul 24	RDGEO2	VLBA	3
1995 Oct 2	RDGEO3	VLBA	3
1995 Oct 12	BF012	VLBA	2
1996 Apr 23...........................	BE010a	VLBA	3
1997 Jan 10...........................	BF025a	VLBA	4
1997 Jan 11...........................	BF025b	VLBA	4
1997 Jan 30...........................	RDV01	VLBA+GcGnKkMcOnWf	3
1997 Mar 31	RDV02	VLBA+GcGnKkMcOnWf	3
1997 May 19...........................	RDV03	VLBA+GcGnKkMcOnWf	3
1997 Jul 24	RDV04	VLBA+GcGnKkMcOnWf	3
1997 Sep 8	RDV05	VLBA+GcGnKkOnWf	3
1997 Dec 17	RDV06	VLBA+GcGnKkMcOnWf	3
1998 Feb 9.............................	RDV07	VLBA+GcGnKkMcNyOnWf	3
1998 Apr 15...........................	RDV08	VLBA+GcGnKkMcNyOnWf	3
1998 Jun 24	RDV09	VLBA+GcGnKkMcNyOnWf	3
1998 Aug 10...........................	RDV10	VLBA+GcGnKkMcNyOn	3
1998 Dec 21	RDV12[a]	VLBA+GcGnKkMcNyWf	3

NOTE.—Gc: Gilcreek, Fairbanks, AK, USA; Gn: NRAO 20 cm, Green Bank, WV, USA; Kk: Kokee, Kokee Park, HI, USA; Mc: Medicina, Medicina, Italy; Ny: Ny Alesund 20 cm, Ny Alesund, Norway; On: Onsala 60 cm, Onsala, Sweden; Wf: Westford, Westford, MA, USA.

[a] RDV12 is not technically contiguous with RDV10, but since only the single experiment RDV11 is missing in between, we chose to include RDV12 in this paper. At the time of this writing the next experiment in the RRFID after RDV12 is RDV31 from 2002 January 16.

REFERENCES.—(1) Fey et al. 1996; (2) Fey & Charlot 1997; (3) RRFID (see footnote 5 of main text); (4) Fey & Charlot 2000.

seven geodetic antennas (Gilcreek: Fairbanks, AK, USA; NRAO 20 cm: Green Bank, WV, USA; Kokee: Kokee Park, HI, USA; Medicina: Medicina, Italy; Ny Alesund 20 cm: Ny Alesund, Norway; Onsala 60 cm: Onsala, Sweden; and Westford: Westford, MA, USA). Eight intermediate frequencies (IFs) were recorded simultaneously, each 8 MHz wide, with four at S band (2.24, 2.27, 2.36, and 2.38 GHz) and four at X band (8.41, 8.48, 8.79, and 8.90 GHz) for a total bandwidth of 32 MHz in each frequency band. Observations were made in a dual-frequency bandwidth synthesis mode to facilitate delay measurements for geodesy and astrometry. The multiplicity of channels allows for the determination of a precise group delay (Rogers 1970), while simultaneous observations in two bands allow for an accurate calibration of the frequency-dependent propagation delay introduced by the ionosphere. Results of the precise geodesy and astrometry afforded by these observations has been presented elsewhere (e.g., Petrov & Ma 2003; Fey et al. 2004). Observations in this mode also allow simultaneous dual-frequency imaging, which is the focus of the work discussed here. Of order 100 sources are observed in a single 24 hr experiment, for an average time on source per experiment of about 15 minutes. This time on source is divided into scans of a minute to a few minutes in length that are spread throughout the 24 hr observing period.

Table 1 shows the 19 VLBA experiments that are included in this paper. As can be seen from this table, the earlier experiments (1994–1996) are spaced more sporadically in time and used only the 10 station VLBA. The later VLBA experiments, corresponding with the beginning of the RDV series in 1997, are spaced roughly every 2 months in time, and these used the full VLBA plus up to seven geodetic antennas. The RDV experiment series has continued to observe every 2 months through the present (and is currently up to RDV57), but the epochs after RDV12 are not yet fully integrated into the RRFID.

The sample selection for this paper was chosen as the set of all sources that were observed at three or more epochs in the VLBA experiments listed in Table 1. Since this paper is primarily concerned with measuring the jet apparent speeds, we considered only the 8 GHz images in this paper, saving the lower resolution 2 GHz observations for future papers. These selection criteria yielded a sample of 87 sources with a total of 966 8 GHz images. The best-observed sources were observed at all 19 epochs, and the average number of epochs per source is 11. The list of the 87 sources in the current RRFID kinematic survey is given in Table 2. This table gives the name of the source in IAU format, other common names, the number of VLBI epochs in the RRFID kinematic survey, the redshift if known, and the source optical type (BL Lac object, quasar, or galaxy) from the Véron-Cetty & Véron (2003) catalog.

3. DATA ANALYSIS

3.1. *AIPS Calibration*

The raw data bits were correlated with the VLBA correlator at the Array Operations Center in Socorro, New Mexico, USA. The correlated data were calibrated and corrected for residual delay and delay rate using the NRAO Astronomical Image Processing System (AIPS). Initial amplitude calibration for each of the eight IFs was accomplished using system temperature measurements taken during the observations combined with station-supplied gain curves. Fringe fitting was done in AIPS using solution intervals equal to the scan durations and a point-source model in all cases. After correction for residual delay and delay rate, the data were written to FITS disk files. All subsequent processing was carried out using the Caltech VLBI imaging software, primarily DIFMAP.

3.2. *Imaging*

The visibility data for each frequency band were self-calibrated, Fourier-inverted, and cleaned using the CLEAN algorithm of

TABLE 2
Sources in the RRFID Kinematic Survey

Source	Common Name	Number of Epochs	Optical Class[a]	z	Source	Common Name	Number of Epochs	Optical Class[a]	z
0003−066		12	B	0.35	1128+385		15	Q	1.73
0014+813		12	Q	3.37	1144−379............		10	Q(HP)	1.05
0048−097		15	B	...	1145−071............		12	Q	1.34
0059+581		14	Q[b]	0.64	1156+295		12	Q(HP)	0.73
0104−408		10	Q	0.58	1219+044		11	Q	0.97
0111+021.............		8	B	0.05	1228+126	M87	12	G	0.004
0119+041		14	Q(HP)	0.64	1253−055	3C 279	3	Q(HP)	0.54
0119+115.............		12	Q(HP)	0.57	1255−316		5	Q	1.92
0133+476		13	Q(HP)	0.86	1300+580		9	U	...
0146+056		4	Q	2.35	1308+326		15	Q(HP)	1.00
0201+113		13	Q	3.61	1313−333		12	Q	1.21
0202+149		13	G	0.41	1334−127		13	Q(HP)	0.54
0229+131		15	Q	2.06	1351−018		7	Q	3.71
0234+285		13	Q(HP)	1.21	1357+769		15	Q[b]	...
0238−084	NGC 1052	10	G	0.005	1404+286	OQ 208	11	G	0.08
0336−019	CTA 26	13	Q(HP)	0.85	1418+546		8	B	0.15
0402−362		10	Q	1.42	1424−418		8	Q(HP)	1.52
0430+052	3C 120	11	G	0.03	1451−375		9	Q	0.31
0454−234		14	Q(HP)	1.00	1514−241		11	B	0.05
0458−020		12	Q(HP)	2.29	1606+106		14	Q	1.23
0528+134		14	Q	2.06	1611+343		13	Q	1.40
0537−441		10	Q(HP)	0.89	1622−253		13	Q	0.79
0552+398		18	Q	2.37	1638+398	NRAO 512	14	Q(HP)	1.66
0556+238		8	U	...	1652+398	Mrk 501	3	B	0.03
0642+449		12	Q	3.40	1726+455		10	Q	0.72
0718+793		4	U	...	1739+522		14	Q(HP)	1.38
0727−115............		19	Q	1.59	1741−038		15	Q(HP)	1.05
0742+103		9	G[b]	2.62	1745+624		12	Q	3.89
0749+540		3	B	...	1749+096		19	Q(HP)	0.32
0804+499		13	Q(HP)	1.43	1803+784		12	Q(HP)	0.68
0805+410		3	Q	1.42	1908−201		11	Q	1.12
0823+033		14	B	0.51	1921−293		14	Q(HP)	0.35
0851+202	OJ 287	15	B	0.31	1928+738		3	Q	0.30
0919−260		12	Q	2.30	1954−388		11	Q(HP)	0.63
0920−397		10	Q	0.59	1958−179		3	Q(HP)	0.65
0923+392	4C 39.25	14	Q	0.70	2052−474		4	Q	1.49
0953+254	OK 290	8	Q	0.71	2136+141		8	Q	2.43
0955+476		14	Q	1.87	2145+067		19	Q	0.99
1004+141		9	Q	2.71	2200+420	BL Lac	12	B	0.07
1022+194		3	Q	0.83	2230+114	CTA 102	6	Q(HP)	1.04
1034−293		13	Q(HP)	0.31	2234+282		14	Q(HP)	0.80
1044+719		14	Q	1.15	2243−123		12	Q(HP)	0.63
1101+384	Mrk 421	12	B	0.03	2255−282		11	Q	0.93
1124−186............		12	Q	1.05					

[a] Optical class from Véron-Cetty & Véron (2003). Q = quasar, B = BL Lac object, G = galaxy, HP = high polarization, U = unidentified.
[b] ID from NED (source not in the Véron-Cetty & Véron [2003] catalog).

DIFMAP in an automatic mode. DIFMAP combines the visibilities for each IF of an observation in the (u, v)-plane during gridding, taking into account frequency differences. However, DIFMAP makes no attempt to correct for spectral index effects. The spanned bandwidths of the four IFs in each band are 0.1 GHz (6% fractional bandwidth) at S band and 0.5 GHz (6% fractional bandwidth) at X band, so it is possible that spectral index changes in the core or jet components could cause small errors in the fitted component positions, because the model components are assumed to have zero spectral index. We investigated the magnitude of this effect by using the AIPS task UVMOD to generate components of known position and spectral index, sampled with a typical RRFID (u, v)-plane coverage. The typical error introduced for spectral index changes of about 1 in the core is only a few microarcseconds,

confirming that spectral index effects on position measurements are negligible for our relatively small 6% band spread.

After phase self-calibration with a point-source model, the 4 s correlator records were coherently averaged to 12 s records and then edited. Amplitude calibration at each frequency band was improved through observations of a strong, compact source. A single amplitude gain correction factor was derived for each antenna for each IF, based on fitting a simple Gaussian source model to the visibility data of these compact sources after applying only the initial calibration, based on the measured system temperatures and gain curves. Gain correction factors were calculated based on the differences between the observed and model visibilities. The resulting set of amplitude gain correction factors was then applied to the visibility of all sources. The absolute flux density scale of
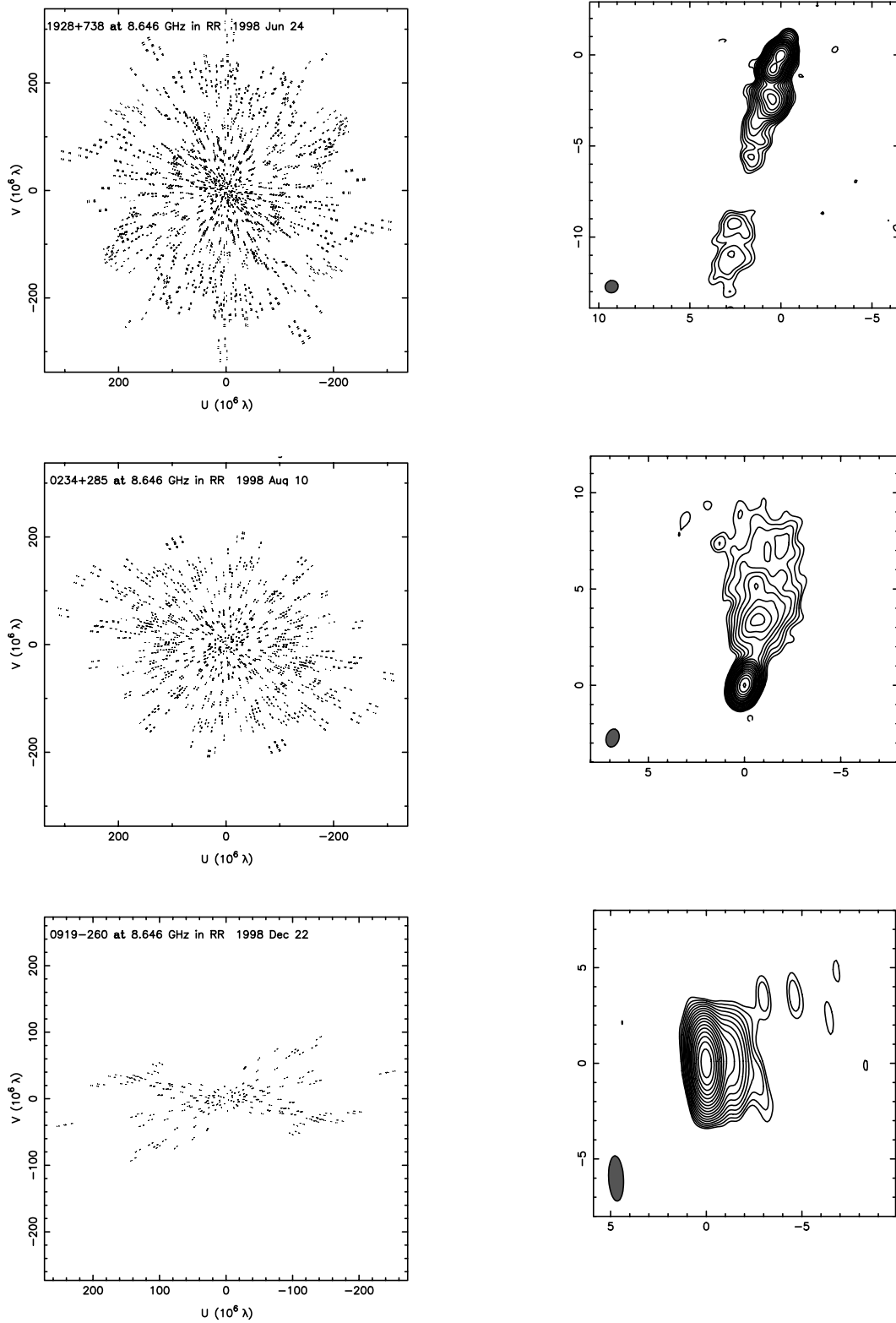
FIG. 1.—Sample (u, v)-plane coverages and associated images for a high-declination (1928+738), medium-declination (0234+285), and low-declination (0919−260) source from the RRFID. Image axes are in milliarcseconds. For 1928+738 the image parameters are: lowest contour 4.3 mJy beam^{-1}, peak flux 1.07 Jy beam^{-1}, and beam size 0.72 mas × 0.67 mas in position angle −68°. For 0234+285 the image parameters are: lowest contour 2.8 mJy beam^{-1}, peak flux 1.04 Jy beam^{-1}, and beam size 0.95 mas × 0.66 mas in position angle −17°. For 1928+738 the image parameters are: lowest contour 3.7 mJy beam^{-1}, peak flux 1.25 Jy beam^{-1}, and beam size 2.36 mas × 0.78 mas in position angle 3°. Lowest contours are set to 3 times the rms noise level in the residual maps. All other contours are factors of $\sqrt{2}$ higher than the previous contour.

TABLE 3
GAUSSIAN MODELS

Source (1)	S^a (Jy) (2)	r^b (mas) (3)	P.A.^{b} (deg) (4)	a^c (mas) (5)	$(b/a)^c$ (6)	ϕ^c (deg) (7)	Type^d (8)	Epoch (9)	Comp.^{e} (10)	a_{beam}^f (mas) (11)	b_{beam}^f (mas) (12)	θ_{beam}^f (deg) (13)
0003−066	1.599	0.079	148.3	0.633	0.387	−16.3	1	1995.78	0	2.29	0.95	−1.1
	0.645	1.040	−60.5	1.384	1.000	0.0	1	1995.78	3	2.29	0.95	−1.1
	0.156	5.145	−74.5	3.222	1.000	0.0	1	1995.78	1	2.29	0.95	−1.1
	1.209	0.032	114.2	0.529	0.000	21.2	1	1997.08	0	2.03	0.75	−5.8
	0.225	0.786	−48.9	0.520	1.000	0.0	1	1997.08	3	2.03	0.75	−5.8
	0.194	2.131	−71.1	1.416	1.000	0.0	1	1997.08	2	2.03	0.75	−5.8
	0.083	5.586	−75.2	2.455	1.000	0.0	1	1997.08	1	2.03	0.75	−5.8

NOTES.—Table 3 is published in its entirety in the electronic edition of the *Astronomical Journal*. A portion is shown here for guidance regarding its form and content.
[a] Flux density of the component.
[b] The r and P.A. values are the polar coordinates of the Gaussian center. P.A. is measured from north through east.
[c] The a and b values are the FWHM of the major and minor axes of the Gaussian, and ϕ is the position angle of the major axis.
[d] Component type for the DIFMAP modelfit command. Type 1 indicates a Gaussian component.
[e] Component 0 indicates the presumed core. Other components are numbered from 1 to 6, from the outermost component inward. A component ID of 99 indicates a flagged component not used in the analysis.
[f] The a_{beam}, b_{beam}, and θ_{beam} values are the major axis FWHM, minor axis FWHM, and position angle of the major axis of the naturally weighted restoring beam.

the data has not been investigated but is estimated to be within 10%–20%.

The data were self-calibrated following the hybrid-mapping technique (Pearson & Readhead 1984) to correct for residual amplitude and phase errors. The data were initially phase self-calibrated and mapped using uniform weighting in the (u, v)-plane before switching to natural weighting after several iterations. A point-source model was used as a starting model for the iterative procedure in all cases. Convergence was defined basically as the iteration when the peak in the residual image became less than a specified factor times the root mean square (rms) noise of the residual image from the previous iteration. Sources with emission
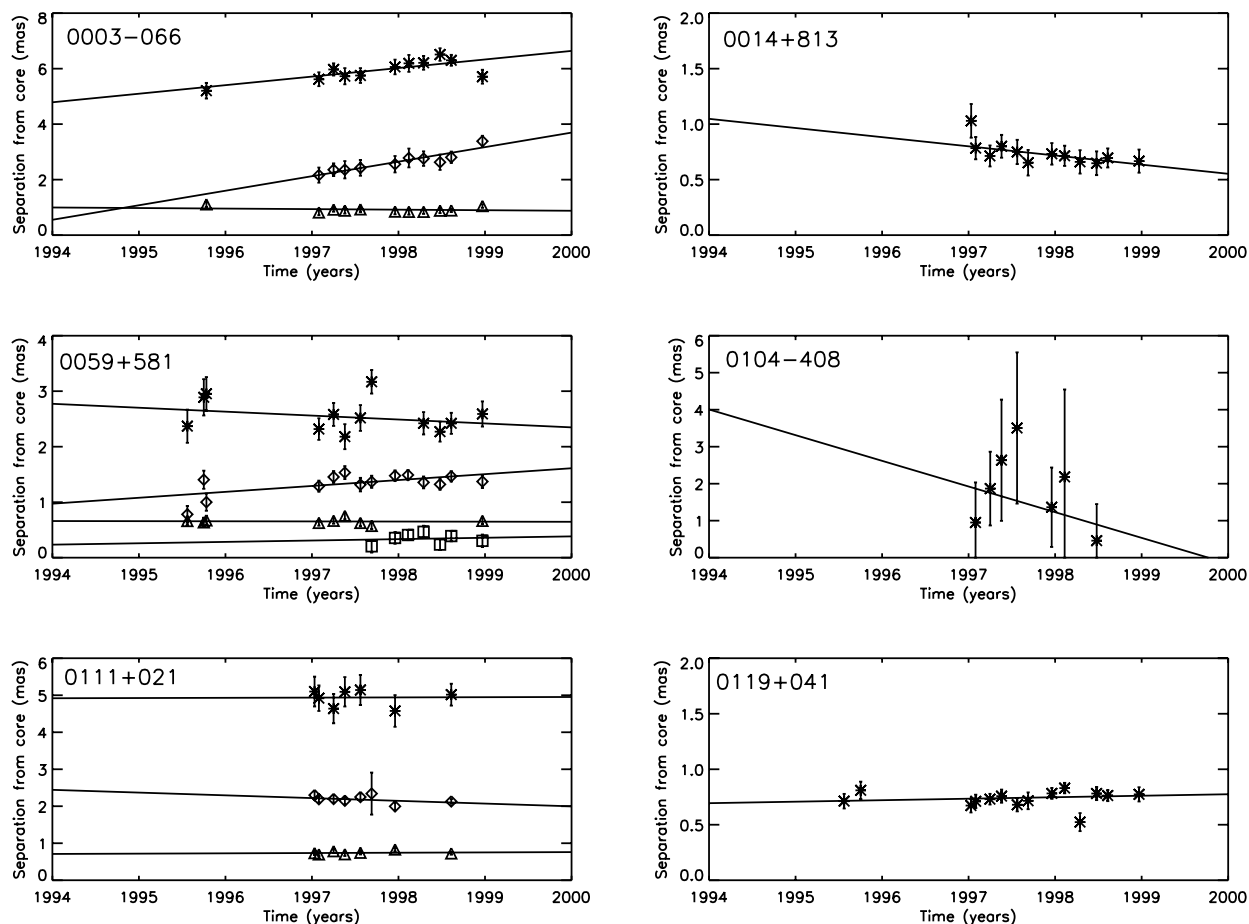

FIG. 2.—Distances from the core of Gaussian component centers as a function of time. The lines are the least-squares fits to outward motion with constant speed. For each source, asterisks are used to represent component 1, diamonds for component 2, triangles for component 3, squares for component 4, crosses for component 5, and circles for component 6. Some error bars are smaller than the plotting symbols.
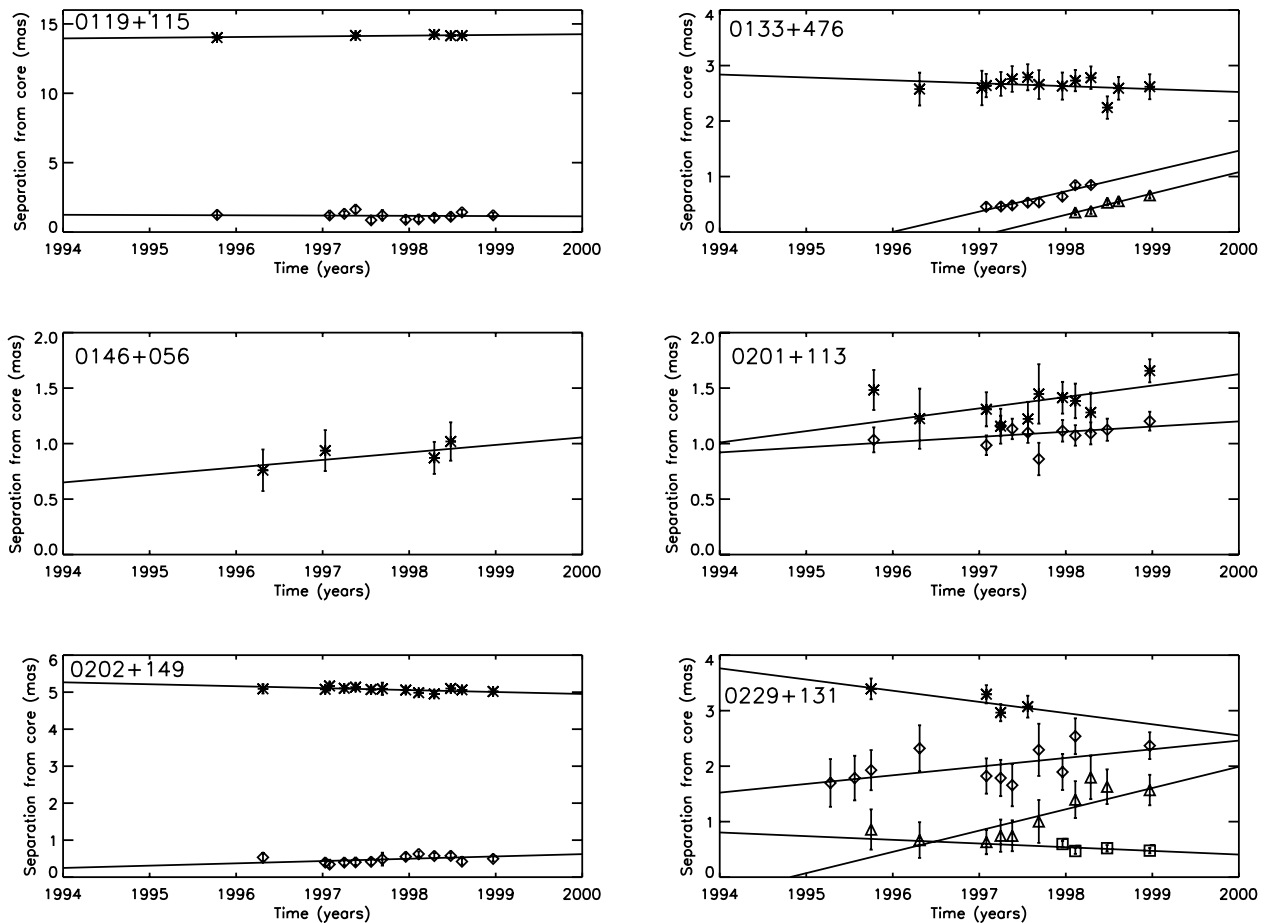
Fɪɢ. 2—*Continued*

structure too complex or too extended for the automatic imaging script to handle were imaged by hand, i.e., in an interactive mode, following the same prescription as that for the automatic mode. Convergence for these sources was subjective and was based on the iteration at which it was judged that further self-calibration would not significantly improve the resultant image.

Far too many VLBA images (966 in total) were used for this paper to present them all in printed form here. A subset of the RRFID images used in this paper has been presented in printed form by Fey et al. (1996) and Fey & Charlot (1997, 2000). In addition, the final CLEAN images are all publicly available from the RRFID (see footnote 5). In Figure 1 we show a sample of three (u, v)-plane coverages along with their corresponding images, in order to show typical (u, v)-plane coverages obtained for high-, medium-, and low-declination sources, respectively.

Because a major section of this paper is a comparison of our jet apparent speed measurements with the 2 cm survey speed measurements for the sources in common, we compare here the factors that influence the image dynamic range and angular resolution in these two surveys. The VLBA beam size is about a factor of 2 larger at 8 GHz than at 15 GHz; thus, the RRFID images that are VLBA-only (the first eight epochs in Table 1) have about a factor of 2 worse angular resolution than the 2 cm survey images. However, the global VLBI beam size at 8 GHz is approximately equal to the VLBA beam size at 15 GHz, so that the later epochs in the RRFID that used global VLBI networks have similar angular resolution to the 2 cm survey observations. The RRFID observations use about one-quarter of the time on source and half the bandwidth of the 2 cm survey obser-

vations, and this implies a loss of sensitivity by a factor of a few relative to the 2 cm survey. However, these factors are compensated for by the greater number of antennas in most of the RRFID observations, the lower SEFD (system equivalent flux density) of the antennas at 8 GHz relative to 15 GHz, and the higher flux of the jet components at 8 GHz. The result of all of these factors is that the dynamic range of the jet detections in the two surveys is similar. Because of their very different setups, it is fortuitous that the RRFID images and the 2 cm survey images are similar in angular resolution and jet dynamic range; this similarity greatly facilitates the comparisons between the results of the two surveys in § 5.

3.3. *Model Fitting*

Gaussian models were fit to the self-calibrated *visibility data* on a source-by-source basis using DIFMAP in an interactive mode. The number of Gaussian components and the choice between elliptical components or circular components was subjective, but motivated by consideration of the simplicity of the resulting model. Thus, elliptical components were used sparingly, and only to represent the core or a very bright jet component when the residuals remaining from a circular Gaussian fit were so large as to hinder further model fitting using the residual map. Although the agreement between the fitted models and the data is not as good as that produced by the hybrid images (models with many CLEAN components), inspection of plots of residuals in the image plane, after subtracting the Gaussian models from the visibility data, revealed that the Gaussian models generally describe the visibility data quite well. However, because of incomplete sampling in the (u, v)-plane, these models may not be unique. They
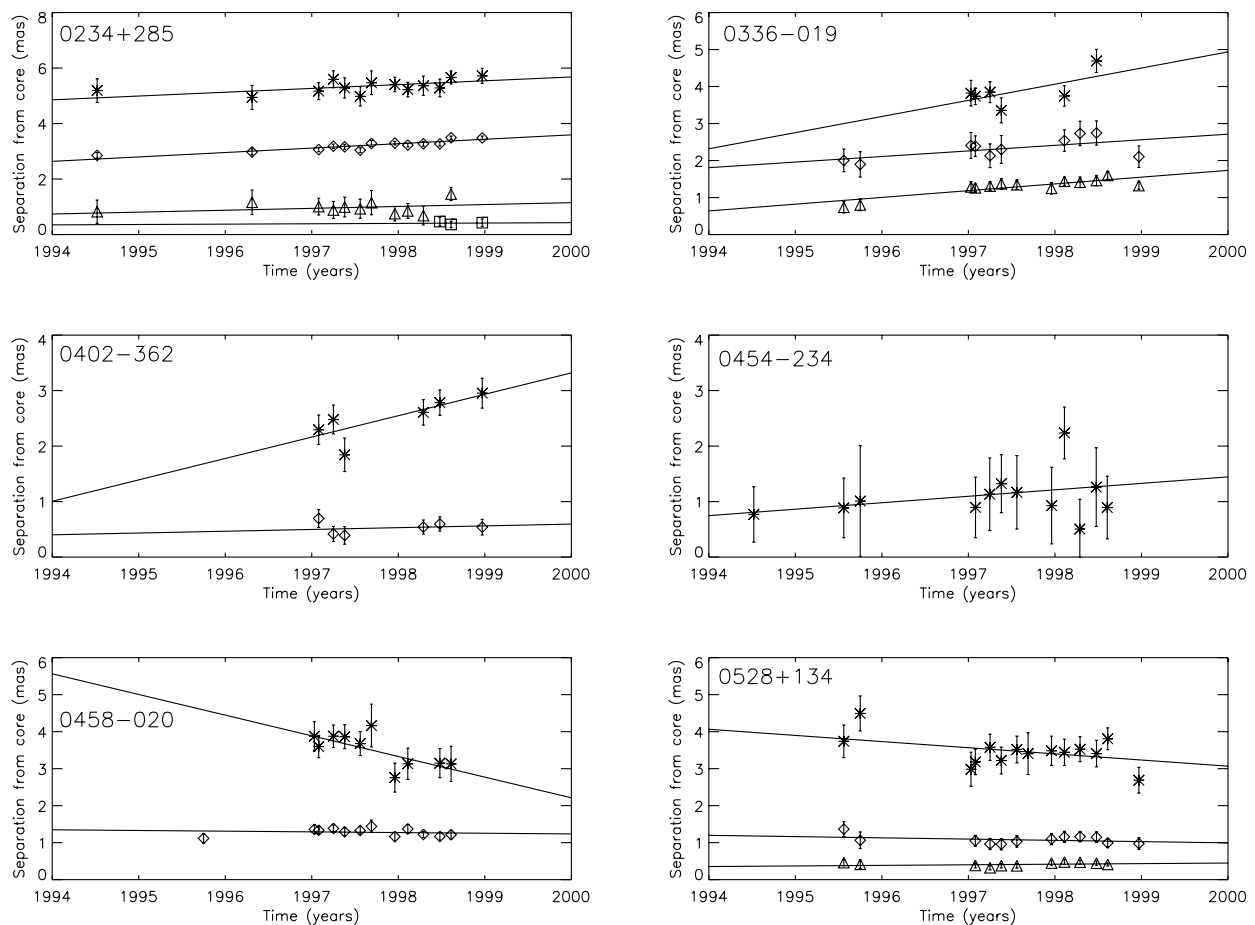
Fig. 2—*Continued*

represent only one *possible* deconvolution of complex source structure. Such deconvolutions can be misleading.

The models were fit to the self-calibrated visibility data corresponding to the publicly available images in the RRFID; no further processing of the visibility data was performed, so others should be able to reproduce the models given here from the publicly available data. The models published here were done independently from the previously published models of five epochs of RRFID data by Fey et al. (1996) and Fey & Charlot (1997, 2000), because it was desired that all model fits be done in a uniform manner for this paper. A comparison of the model fits for those five epochs that were previously fit by Fey et al. (1996) and Fey & Charlot (1997, 2000) shows that in the vast majority (∼90%) of cases there is agreement in the fitted positions of common components within the errors. Any difference between these model fits lies in the presence of an additional component or components in either of the fits; i.e., any difference results from a differing decision of when to stop adding components to the residual map, and in these cases one model is basically a subset of the other. In a small number (∼10%) of cases the corresponding model fits give significantly different component positions; these are cases where multiple deconvolutions of the source structure are possible, and such cases are discussed further in the context of comparisons with the 2 cm survey results in § 5.

The model fits for the entire RRFID kinematic survey to date are presented in machine-readable form in Table 3, which contains a total of 2579 Gaussian components and should be suitable for script-based processing by other investigators. Some sources

listed in Table 2 do not have model fits given in Table 3, for the following reasons.

1. Lack of *z*: six sources (0048−097, 0556+238, 0718+793, 0749+540, 1300+580, and 1357+769) did not have a measured redshift at the time of this writing. Because no apparent speed could be determined for these sources, we did not model them.

2. Complexity: three sources (0238−084, 0430+052, and 1404+286) had 8 GHz structures that were two sided (hindering identification of the core) and/or so smooth and complex at 8 GHz that we were not able to reliably follow components from epoch to epoch.

3. Lack of a jet: one source (2052−474) was modeled as only a core component at all epochs.

In all, 77 of the 87 sources listed in Table 2 have model fits in Table 3.

Columns (2)–(8) of Table 3 correspond directly to the DIFMAP `modelfit` results and are suitable for reading directly into DIFMAP with the `rmodel` command. Positions in Table 3 have *not* been shifted to place the core at the origin so that they will correspond directly to positions on the publicly available RRFID images. Column (10) of Table 3 contains the component identification, the core is identified as component 0, and other jet components are identified as components 1–6, from the outermost component inward. We identify the core in each source as the compact component at the end of the one-sided jet structure; often, but not always, it is also the brightest component. As noted above, we excluded any sources known to show two-sided VLBA structures at
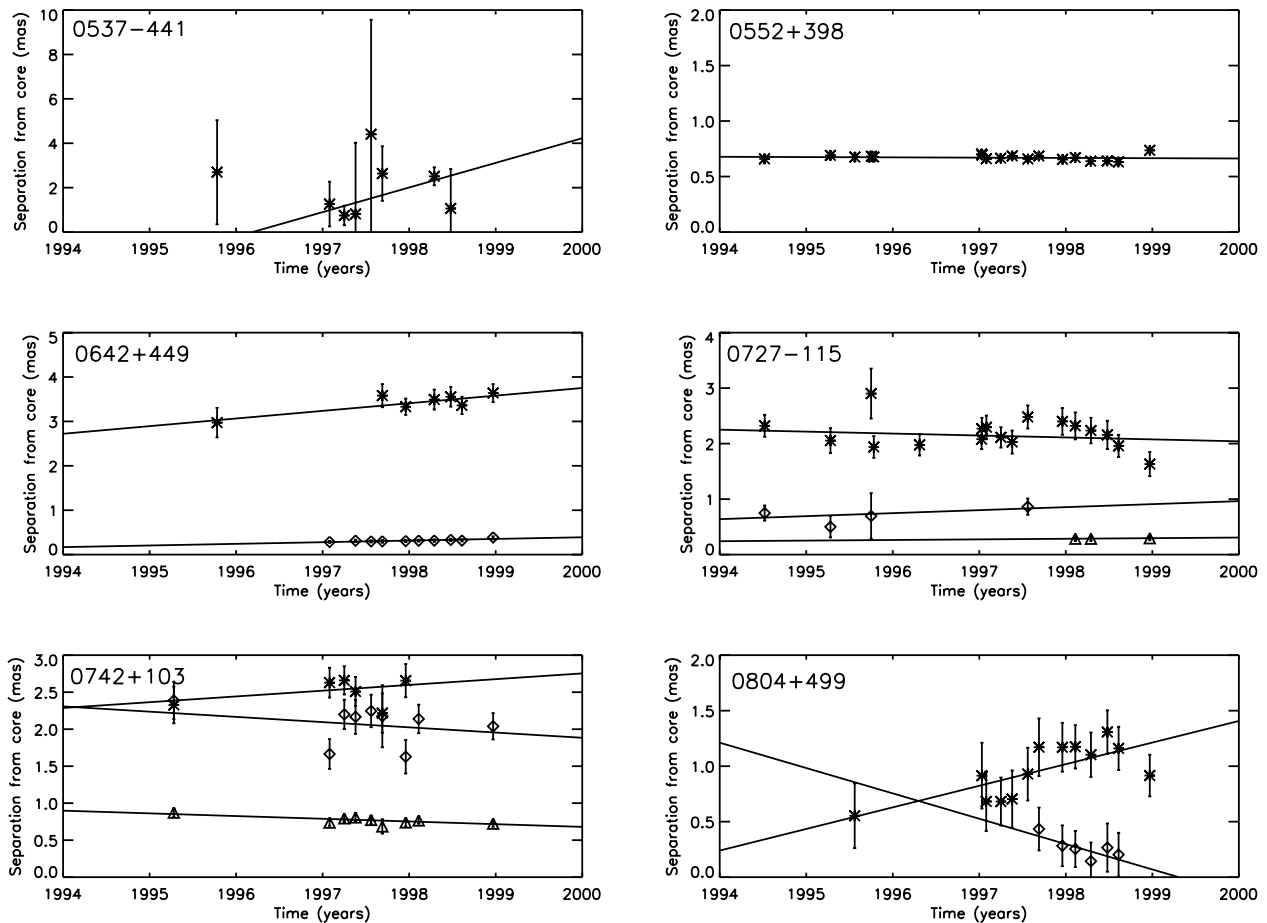
Fig. 2—*Continued*

these scales. Identifications of other components from epoch to epoch were done through continuity in radial position, flux, and position angle; this was facilitated by the dense time coverage of the RRFID during 1997 and 1998. However, we note that often the identification scheme adopted represents what we considered to be the most likely of several possible scenarios, and that different identification scenarios can lead to different measured jet properties. In cases where a model component could not be directly identified with model components seen at other epochs (about 5% of the total fitted components), it was given an identification of 99 in Table 3 to flag it as a model component not used in the analysis. This typically happened when a somewhat lower resolution image blended together what was seen as two separate components in other model fits, or when an extended low-dynamic-range component was detected in only a few images with a poorly constrained position.

All components were modeled as Gaussians (the only extended brightness distribution fully supported in DIFMAP), and it is worth considering whether assuming a different brightness distribution would have any effect on the measured apparent speeds. We investigated this by modeling a test source (chosen to be 1308+326 because of the very small scatter of the measured Gaussian component positions about the best-fit line) a second time with an alternate brightness distribution; the core was modeled as a uniformly bright disk, and the single-jet component as an optically thin sphere. The measured apparent speed differed by about 5% between the two cases, but considering the errors on the fit, this difference was not significant. Where the assumed brightness distribution will have a large effect is on the measured

sizes of the components (Pearson 1995), but the measured sizes are not used in this paper.

4. RESULTS

4.1. *Apparent Speeds*

Apparent radial proper motions for the jet components in Table 3 were derived from linear least-squares fits to the separation of the jet components from the VLBI core versus time, for components that were observed at three or more epochs. The proper motions were then converted to apparent radial speeds using the cosmology given in § 1. These fits are shown in Figure 2, and the results are tabulated in Table 4. A total of 184 component motions in 77 sources are tabulated in Table 4. Note that the disappearance of a component on Figure 2 followed by its reappearance at later epochs does not imply the literal disappearance and reappearance of the component on the images. Rather, the component is usually present at a marginally significant level in the intervening images, but is not significant enough to have its properties well constrained by the model fitting.

Errors on the fitted radial positions of model components were estimated by examining the scatter in the model-fit positions between sources present in the two pairs of adjacent epochs 1995 October 2–12 and 1997 January 10–11. A total of seven common sources with 16 common components are present in either of these epoch pairs. The epochs comprising these two pairs are close enough together in time that actual component motions are negligible, and any scatter in the fitted positions represents the statistical errors in the model fits. Figure 3 shows a plot of the
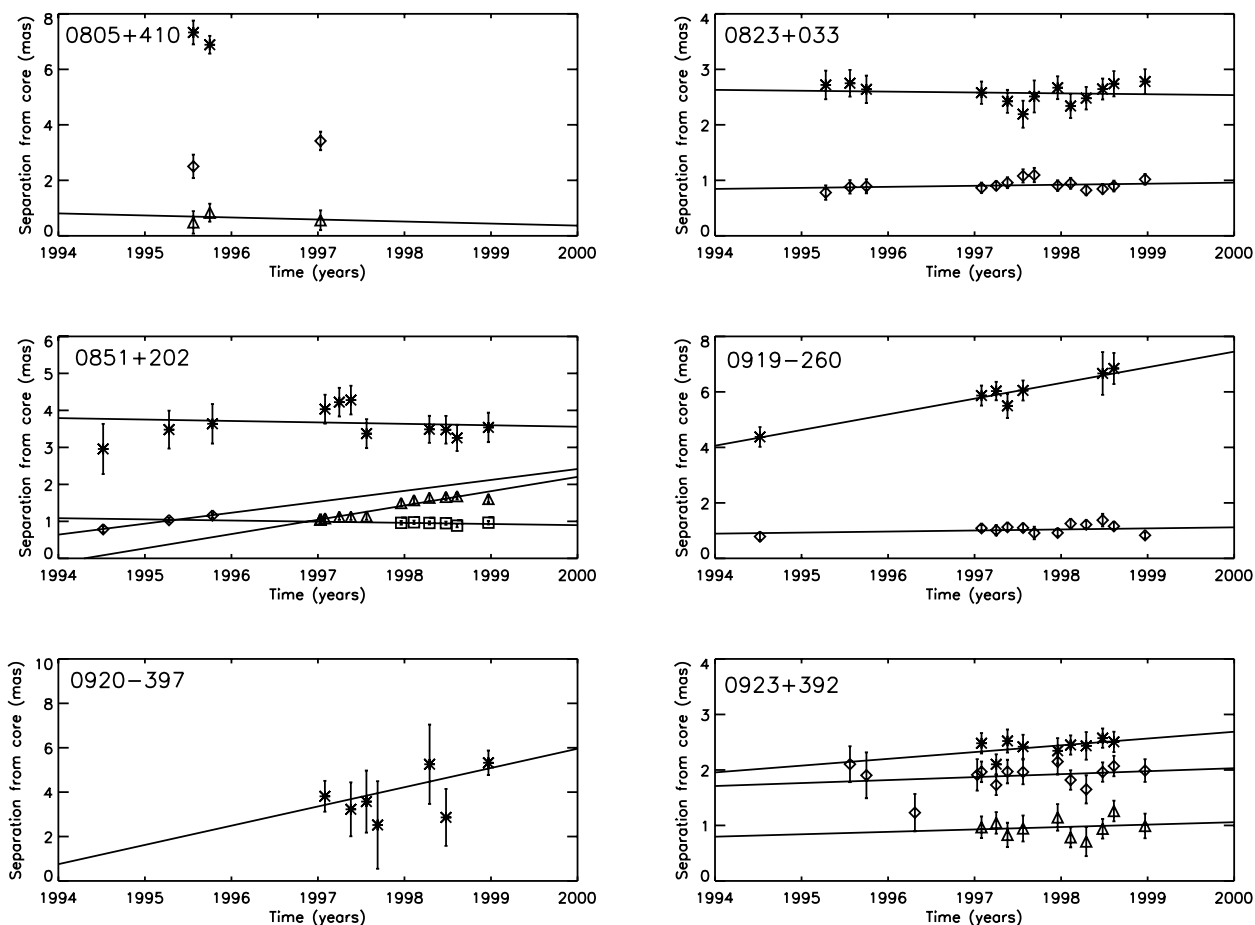
Fɪɢ. 2—*Continued*

difference in the fitted radial positions of the common components in these two epoch pairs (expressed as a fraction of the beam size in the radial direction, because we expect the scatter to be proportional to the beam size) versus the component flux (averaged between the two epochs). The positions of brighter components should be more accurately determined relative to the beam size, and we expect a plot such as Figure 3 to show an upper envelope. Figure 3 does appear to show such an envelope, and a fit of a power law in flux to the eight points near the upper envelope (*asterisks*) gives a fit close to $\Delta r \approx 2S^{-1/2}$, where Δr is measured in beams and S is measured in millijanskys; this curve is plotted as a solid line. Error bars for individual components were estimated based on this curve by setting the error bar size to be a fraction $1/2^{\xi}$ of the beam size, where ξ was set from the upper envelope fit given above as the closest integer to $1/2(\log S/\log 2) - 1$, where S is the average flux of the component, and the maximum value of ξ was 5. The above procedure was used to set the default value for ξ, but since there are other factors that influence the model-fitting accuracy, such as the presence or absence of other confusing components, ξ was adjusted from this default value if the error bars were obviously way too large or too small (based on the significance of the fit), on a case-by-case basis.

We also computed all apparent speeds and associated errors a second time, with no errors applied to the individual position measurements, and the speed error calculated from the dispersion about the linear fit, as was done for the 2 cm survey data by K04. The distributions of apparent speeds obtained by the two fitting methods are statistically nearly identical according to a K-S test, and the two measured speeds for any given component typically

differ by much less than 1 σ. We retain the method described in the previous paragraph, because, while the data in Figure 3 from which the flux dependence is derived are somewhat sparse, it at least takes into account the changing resolutions from the early to the late epochs (which went from VLBA-only to global VLBI; see Table 1) by assigning beam-based errors, and it is consistent with the values obtained from the dispersion about the linear fits.

An inspection of Table 4 shows a significant number of negative apparent speeds (about 25% of component speeds). A negative apparent speed corresponds to inward motion toward the presumed core and would be physically important if convincingly detected. However, all of the negative apparent speeds in Table 4 are under 3 σ significance, and we regard these as most likely due to stationary or slowly moving components that happen to have a formally negative best-fit apparent speed. In fact, when we look at the distribution of significances of the negative apparent speeds, they match closely a normal distribution centered at zero (34% have over 1 σ significance, and 8% have over 2 σ significance), supporting the interpretation in terms of stationary or slowly moving components. Other VLBI surveys have reached similar conclusions regarding components with negative apparent speeds; see, for example, the discussions by K04 and Vermeulen et al. (2003).

Note that there are some apparent speeds listed in Table 4 with extremely large associated errors (e.g., the two components in 1255−316, with formal errors on the measured apparent speeds of about 50c). This has usually occurred because the RRFID is not a survey that was specifically designed to measure jet kinematics, so occasionally a source may be observed for only a few
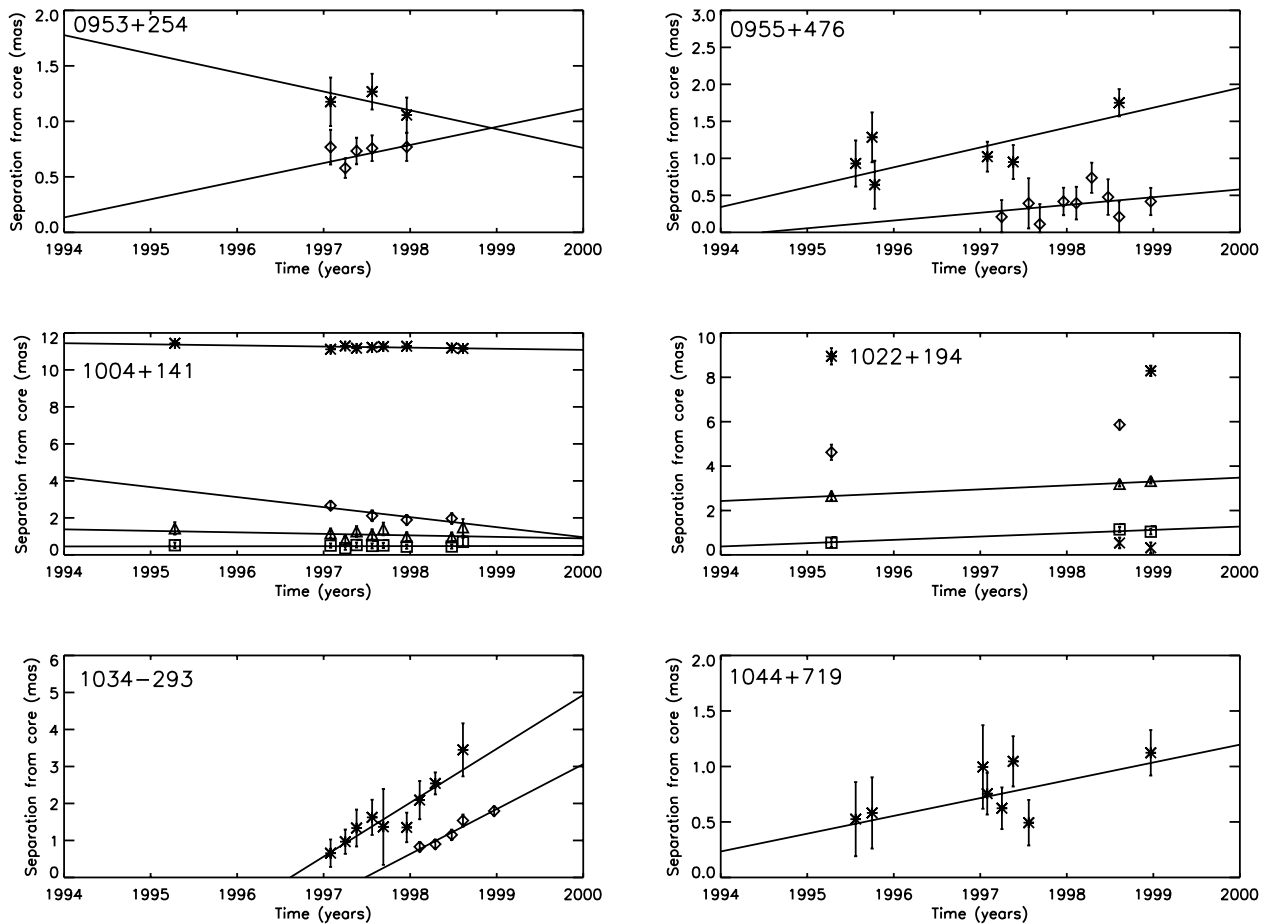
Fig. 2—*Continued*

epochs over a period of a few months. Observing a component over a period of only a few months at 8 GHz yields large errors on the measured apparent speeds. We include these components in Table 4 for completeness, and to show the current state of the RRFID observations of these sources, but we caution that there is little or no information contained in those particular speed measurements, so *they should not be used by anyone for any reason.*

To aid in the comparison to the 2 cm survey presented in § 5, we assigned quality codes to each component motion using the same criteria used by K04. These criteria are:

1. The component is observed at four or more epochs.
2. The component is a well-defined feature in the images.
3. The uncertainty in the fitted proper motion is ≤ 0.08 mas yr^{-1}, or the proper motion has a significance $\geq 5\,\sigma$.

The quality codes are then assigned as follows:

1. "E" (excellent) for motions that satisfy all three of the above criteria.
2. "G" (good) for motions that satisfy any two of the above criteria.
3. "F" (fair) for motions that satisfy only one of the above criteria.
4. "P" (poor) for motions that do not satisfy any of the above criteria, or for motions for which the uncertainty in the fitted proper motion is >0.15 mas yr^{-1} (except for the $\geq 5\,\sigma$ cases mentioned above).

These quality codes are listed in Table 4. Following K04, we restrict subsequent analysis to those components having a "good"

or "excellent" quality code. This selection criterion excludes 90 of the 184 measured apparent speeds in Table 4, leaving a total of 94 apparent speeds in 54 sources that are used in the subsequent analysis. We note that because of the difference between the time baseline of the currently analyzed RRFID data (5 yr) and that of the 2 cm survey (8 yr), our typical uncertainty in fitted proper motions is about a factor of 8/5 larger than the typical uncertainty from K04, causing a smaller yield of "excellent" and "good" components (about 50% of our components) compared to K04 (about 75% of their components), due to the application of criterion (3) above. These uncertainties in fitted proper motions will be reduced as more of the RRFID data is analyzed.

A histogram of the apparent speeds of the 94 "good" and "excellent" components is shown in Figure 4. The mean apparent speed of these components is $3.6c$. The general shape of the distribution is similar to that found by other VLBI surveys, with a peak at the lowest apparent speeds, and a tail extending out to higher speeds, up to about $30c$ in the case of Figure 4. About half of the components are in either the lowest speed or negative speed bins, and these are consistent with being stationary components. Such stationary components are also observed to be common in the other large multiepoch VLBI surveys, including the radio-selected 2 cm and CJF surveys (K04; Vermeulen 1995) and the VLBI survey of EGRET blazars by Jorstad et al. (2001). In each of those surveys, one-third to one-half of the VLBI components observed were found to be slow or stationary ($<2c$ apparent speed when expressed in the cosmology given in § 1). Numerical simulations of relativistic jets also produce such stationary components; for example, the simulations of relativistic
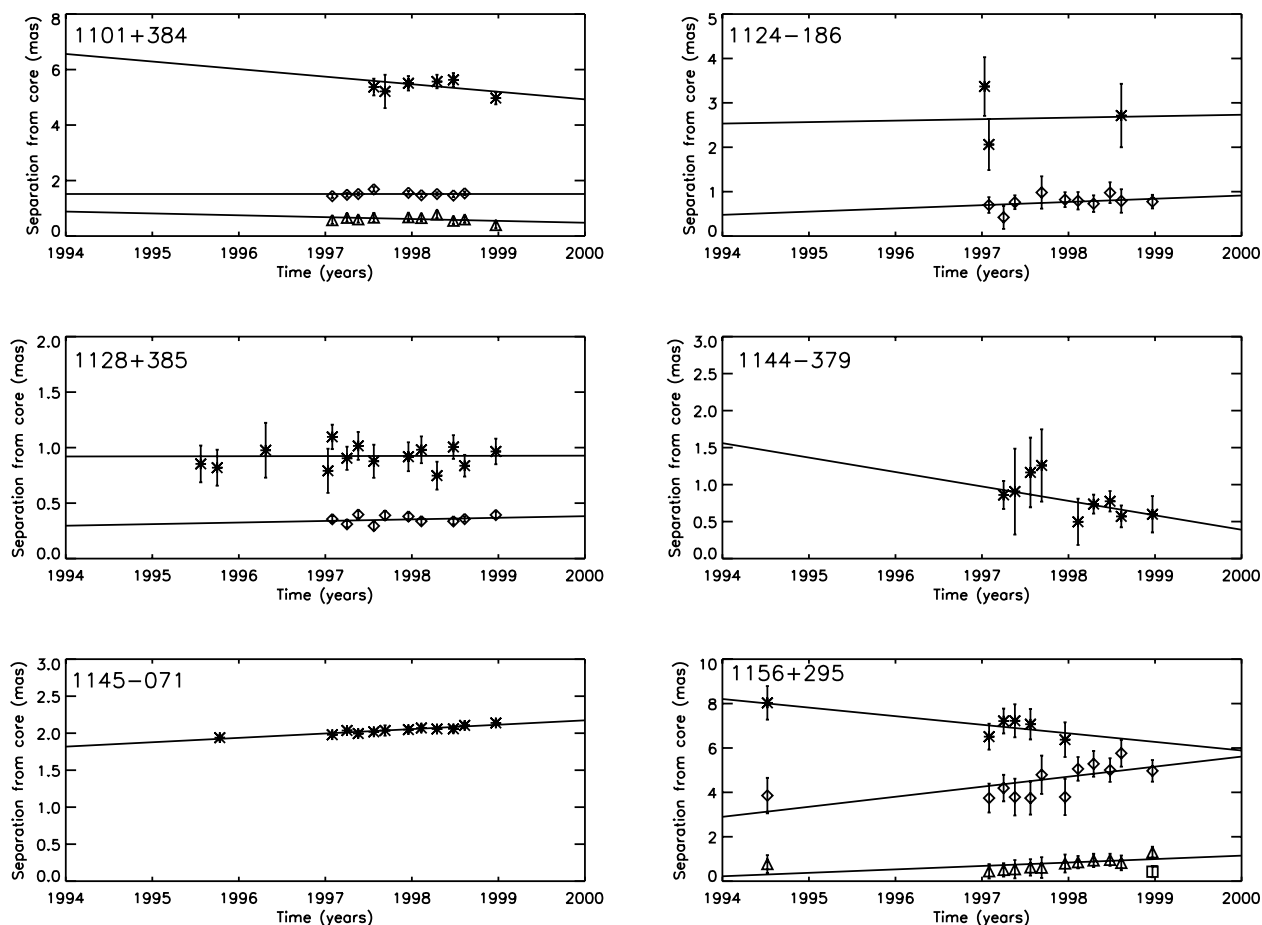
Fig. 2—*Continued*

jets by Gomez et al. (1995) suggested that such stationary components may be standing oblique shocks created by quasi-periodic recollimation shocks. Further simulations by Agudo et al. (2001) suggested that multiple slowly moving conical shocks formed from the interaction of superluminal components with the underlying jet could also produce apparently stationary components on VLBI maps.

We have quantitatively compared the distribution shown in Figure 4 with the apparent speed distributions obtained by other authors using the Kolmogorov-Smirnov (K-S) test. A direct comparison of the histogram in Figure 4 with the corresponding histogram for the 2 cm survey from K04 shows a difference at the 95% significance level; however, this difference is solely the result of the greater scatter toward negative apparent speeds of the presumably stationary components caused by the approximately 8/5 greater statistical uncertainty in the RRFID proper motions mentioned above. If the negative apparent speeds from both surveys are grouped in their respective $0c$ bins, then the K-S test finds no significant difference between the distribution of apparent speeds measured here and that measured by the 2 cm survey. Note that although the general shapes of the overall apparent speed distributions agree quite well between this paper and K04, specific results for some individual sources shared by the two surveys do differ (see § 5 for a full discussion). A K-S test shows a significant difference between the distribution in Figure 4 and the distribution of apparent speeds in EGRET-selected gamma-ray blazars measured by Jorstad et al. (2001) with >99.7% confidence (regardless of what is done with the negative apparent speeds). This type of

difference is expected if the gamma-ray emission is more highly beamed than the radio emission; however, see the further discussion of this issue in § 4.3.

Different components within the same jet can have different apparent speeds, as obviously demonstrated by the coexistence of fast-moving and stationary components in the same source. Approximately one-third of the sources that have multiple components in Figure 4 have apparent speeds that are different from one another at greater than 99% confidence. However, the dispersion of apparent speeds for individual sources is typically less than that for the sample as a whole, as was also found by K04 for the 2 cm survey. For the 27 sources that have multiple components in Figure 4, all but five have a dispersion of their apparent speeds that is less than the dispersion of all components in Figure 4 taken together ($6.9c$). This demonstrates the existence of a "characteristic speed" associated with individual jets. Analysis of correlations between the fastest observed apparent speed in a source and other source properties using the 2 cm and MOJAVE survey samples (Lister 2006) has suggested that the fastest observed pattern speed in a source is a good indicator of bulk apparent speed. The characteristic speed mentioned above may then be the bulk flow speed of the jet, with individual components moving at pattern speeds ranging from zero up to this bulk flow speed. A scenario such as this would be consistent with jet simulations such as those of Agudo et al. (2001), in which primary disturbances moving at the jet flow speed spawn secondary "components" that move at slower pattern speeds (or are stationary). In this interpretation, the maximum apparent speed in a
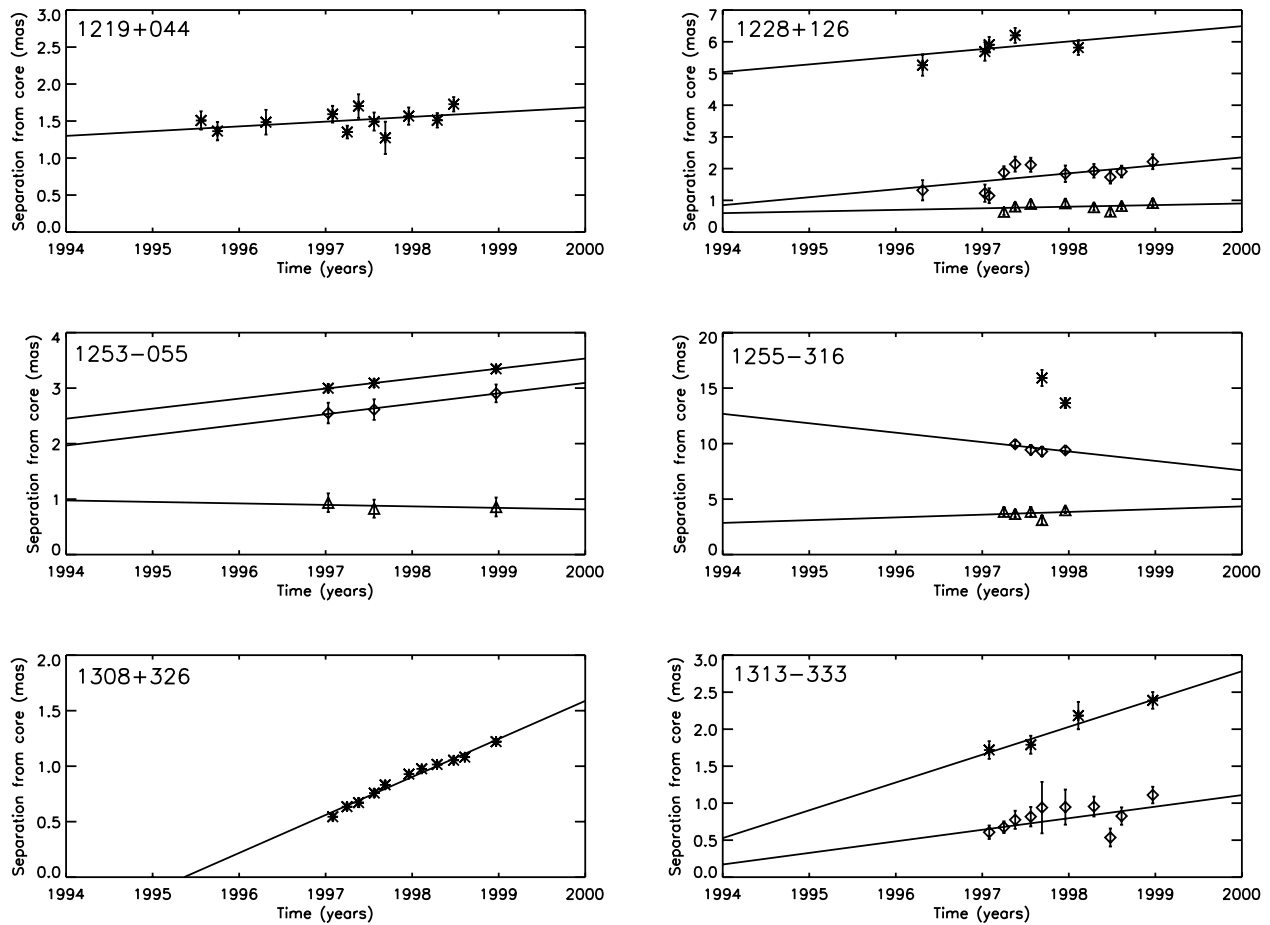
FIG. 2—*Continued*

source, measured over a time interval of many years, would be the most reliable indicator of bulk Lorentz factor. In Figure 5 we show the distribution of maximum apparent speeds for the RRFID sample. The figure shows a histogram of the fastest measured pattern speed in each of the 54 sources represented in Figure 4. The mean fastest apparent speed in a source is 5.9c. Note that an excess of stationary components could still be produced in such a plot if some sources had not yet been observed over a long enough time interval to see a component moving at the apparent bulk speed.

Figure 6 shows the distribution in Figure 5 separated by the optical type given in Table 2 into quasars and BL Lac objects. (Because only three sources in Fig. 5 are classified as galaxies, we do not show a separate histogram for the galaxies.) The mean fastest apparent speed for the quasars is $6.8c \pm 1.1c$, and that for the BL Lac objects is $3.2c \pm 1.5c$. This difference in the means is significant at the 94% confidence level. For comparison, K04 found that their observed apparent speed distributions for quasars and BL Lac objects differed at the 98% confidence level, and Jorstad et al. (2001) found that the apparent speed distributions of EGRET-selected quasars and EGRET-selected BL Lac objects differed at the 99.9% confidence level. Why this difference should be statistically more significant for the groups of gamma-ray-selected quasars and BL Lac objects than for the radio-selected groups is unclear.

4.2. *Apparent Nonradial Motions and Accelerations*

In this subsection, we check for two different types of apparent accelerations in the modeling data. First, we perform second-order fits to r versus t (three free parameters), to check for apparent radial accelerations or decelerations that could be caused by a changing Lorentz factor, angle to the line of sight, or direction of motion. The 13 closely spaced epochs during 1997 and 1998 should give some sensitivity to such second-order terms in the apparent radial motion. Second, we perform first-order fits to x versus t and y versus t (four free parameters), which allows us to fit for a direction of motion of the component that may be different from its mean position angle, or nonradial. With the current time baseline and resolution of the RRFID data, higher order fits with more free parameters do not give meaningful results, although they will as the time baseline of the RRFID continues to be extended in future papers.

We fit all components that were observed at four or more epochs (161 components) with a second-order polynomial for $r(t)$. To check for significant accelerations, we considered all components for which the second-order term had greater than 2 σ significance. There were 17 such components, for which ≈ 8 such $2\,\sigma$ detections are expected by chance alone, suggesting some detections of real accelerations. From those 17 components, we exclude those with "fair" or "poor" quality codes, as well as those for which the extremum of the second-order function occurs within the time range of the component observations. Such fits would represent a component that reverses its direction of motion during the observed time interval—we consider this physically unlikely and expect that these results are caused by a statistically abnormally high or low point or points in the midst of the component position data. There remain three components that we consider to be the most likely detections of radial accelerations: component
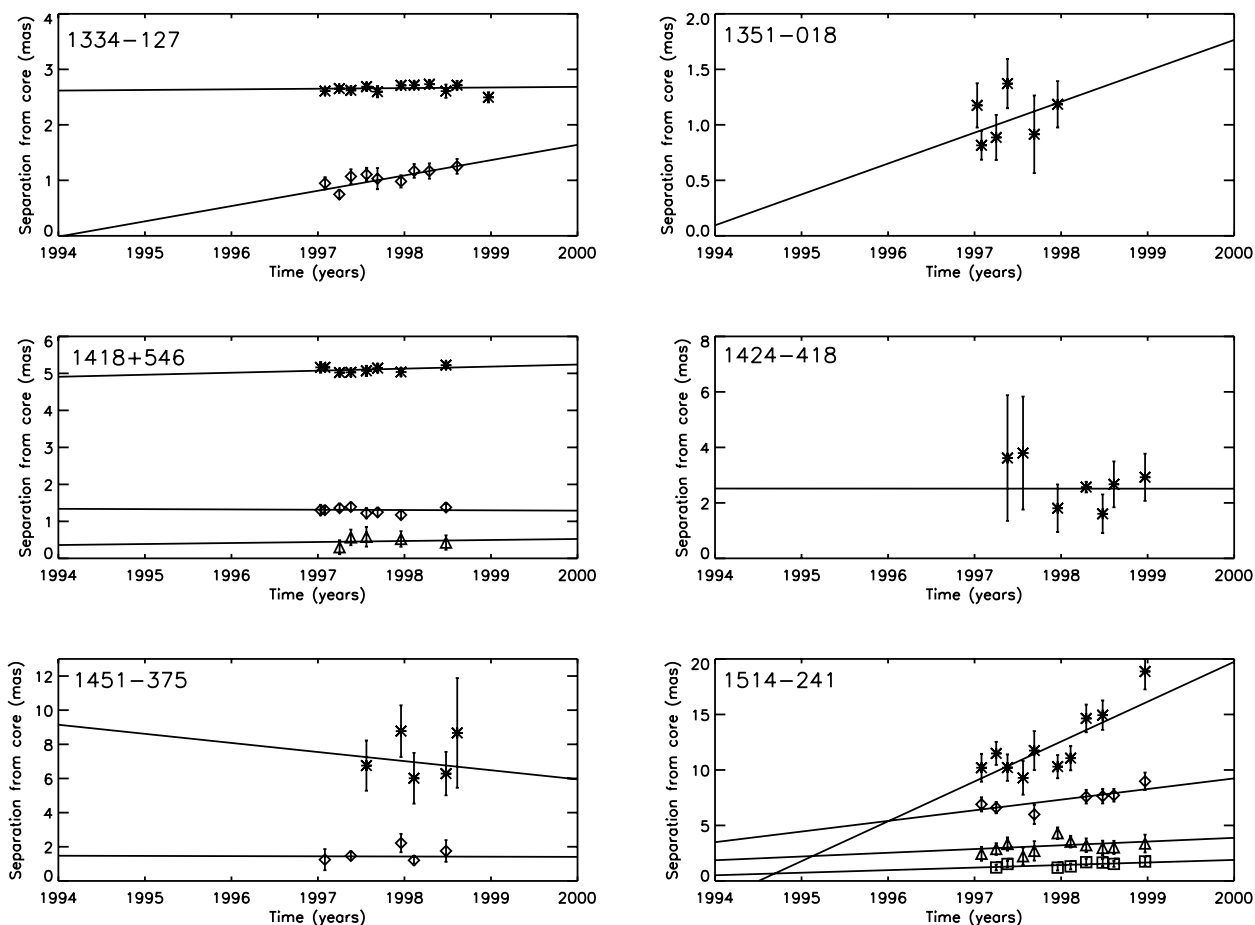
Fig. 2—*Continued*

C2 in 0234+285 ($a = 0.059 \pm 0.028$ mas yr^{-2}), component C1 in 1308+326 ($a = -0.130 \pm 0.051$ mas yr^{-2}), and component C1 in 2200+420 ($a = 0.717 \pm 0.295$ mas yr^{-2}). Two of these accelerations are positive and one is negative. A positive apparent radial acceleration could be due to an increase in the bulk Lorentz factor of the component (as is suggested to occur on parsec scales in some models, such as the accelerating MHD jet model of Vlahakis & Königl 2004), or to a bend toward the critical viewing angle for maximum apparent speed. Negative apparent radial accelerations could be caused by a decrease in the bulk Lorentz factor, a bend away from the critical angle, or a curved trajectory that acquires a significant nonradial component. In fact, two of these three sources do have detectable nonradial motions, as discussed below. These various scenarios will also produce variations in the apparent brightness of the component as the beaming factor changes, but such variations are complicated by not knowing the true viewing angle or intrinsic variability of the component.

The second-order radial fits discussed above are limited to detecting apparent acceleration of a component in the radial direction. In order to check for possible nonradial (nonballistic) trajectories of components, we have also fit first-order linear functions separately to $x(t)$ and $y(t)$, as was also done for the 2 cm survey sources by K04. These fits then determine a direction of motion, as well as the magnitude of the vector velocity. They allow determination of possible nonradial trajectories by comparison of the fitted direction of motion with the average position angle of the component. Such nonballistic trajectories may be caused by flow of the jet plasma along a curving channel, and

such trajectories have previously been detected in numerous individual source studies (dating back to at least Zensus et al. [1995], for quasar 3C 345). For consistency, we use here the same criteria as K04 for determining what constitutes a significant detection of nonradial motion; namely, that the fit must meet the following conditions: the component must be detected in at least five epochs, the vector velocity magnitude must be of at least 5 σ significance, and the fitted direction of motion must differ from the mean position angle of the component by at least 3 σ. A total of 18 components satisfy the first two criteria, and of these, six have significant nonradial motion according to the third criterion. A third of the best-determined motions in the current RRFID sample are nonradial, the same fraction that was found for the 2 cm survey by K04. The fit values for these six components are tabulated in Table 5. Some components that are apparently stationary when only radial motion is considered may turn out to have significant velocity magnitudes when the total velocity is taken into account (e.g., C2 in 0823+033 and C1 in 1611+343). Of the six sources listed in Table 5, five are also in the 2 cm survey (all except for 1622−253), but for 1611+343 and 2136+141 the component listed in Table 5 lies farther out than the components tracked in those sources in the 2 cm survey (K04). For 0234+285, K04 also detected nonradial motion in the same component, and the parameters of the nonradial fits are in good agreement. For 2200+420, K04 detected nonradial motion in the same direction as that listed in Table 5, but in a different component. For 0823+033, our identification of components differs from that by K04 (as discussed further in § 5), so there is no corresponding detection of nonradial
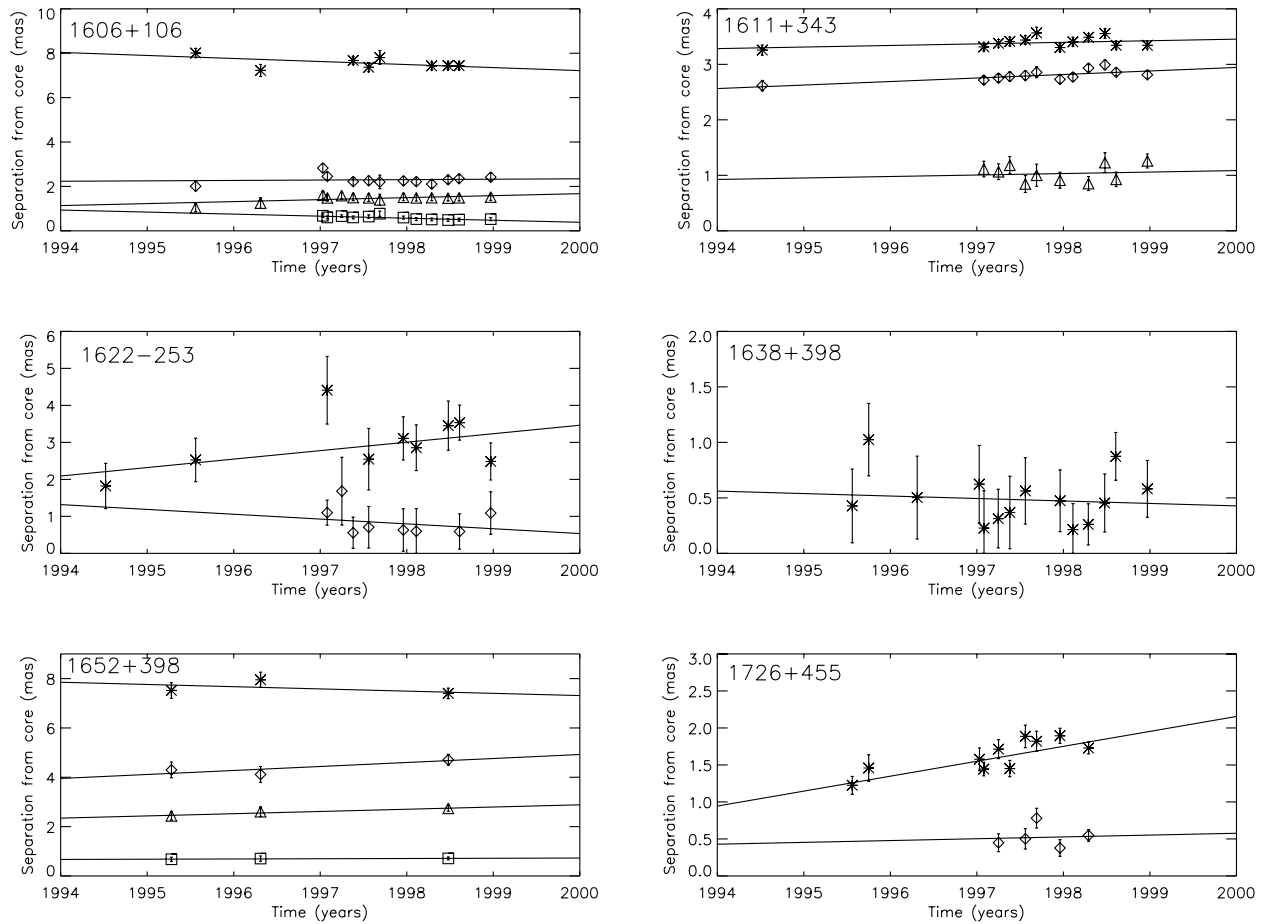
FIG. 2—*Continued*

4.3. *Gamma-Ray Sources*

motion in this source by K04. Regardless of the agreement or lack thereof on specific sources, these two large VLBI surveys agree that roughly one-third of well-measured component trajectories are nonradial, conclusively ruling out a purely ballistic model of the motion of radio-emitting components.

The detection by the EGRET instrument of order 100 blazars at GeV gamma-ray energies (Hartman et al. 1999) opened up a new wavelength region to blazar astrophysics. It is interesting to note that many very bright radio blazars were *not* detected above the EGRET threshold in GeV gamma rays (including, for example, 4C 39.25 from this survey), raising the question of why many radio-loud blazars had strong, detectable gamma-ray emission while others did not. One possible explanation for this is that the gamma-ray and radio emission are relativistically beamed by different powers of the Doppler factor, with the gamma-ray emission being the more highly beamed. This enhancement of Doppler beaming in gamma rays occurs in the synchrotron self-Compton (SSC) model for gamma-ray emission simply because of the steeper spectral index in the gamma-ray portion of the spectrum. In the external-radiation Compton (ERC) model for gamma-ray emission, the beaming enhancement of the gamma-ray emission relative to the radio emission can be even larger (Dermer 1995). If the gamma-ray emission is more highly beamed than the radio emission, then the EGRET blazars should be biased toward higher Doppler factors than radio-selected samples. Assessing the effect of differing Doppler factors on observed ap-

parent speeds is not trivial—interior to the critical angle that maximizes apparent speed the Doppler factor is negatively correlated with apparent speed, while outside this angle the correlation is positive; so one cannot simply conclude that higher Doppler factors produce faster jets. Instead, these effects must be studied through Monte Carlo simulations of the populations under consideration. Simulations by Lister (1999), assuming a linear relation between radio and gamma-ray luminosity, have shown that in a radio-selected flux-limited sample, the EGRET-detected subset should indeed have systematically faster apparent speeds than the nondetections.

A study of the kinematic properties of the EGRET blazar jets was performed by Jorstad et al. (2001), using multiepoch VLBA images at 22 and 43 GHz. By comparing the apparent speeds measured in their study with those measured in the radio-selected CJF sample, Jorstad et al. (2001) concluded that the EGRET sources were significantly faster than the radio-selected sources and therefore more highly beamed. We have confirmed such an apparent speed difference in this paper; as discussed in § 4.1, a K-S test shows that the RRFID apparent speed distribution in Figure 4 differs from the apparent speed distribution for the EGRET blazars in Jorstad et al. (2001) with high significance. However, the measurements by Jorstad et al. (2001) were made at the high linear resolutions afforded by their 22 and 43 GHz observations, and they therefore sampled regions closer to the core than either the CJF survey or the RRFID survey in this paper. Separating possible resolution effects from population effects is problematic, and ideally the gamma-ray and radio-selected
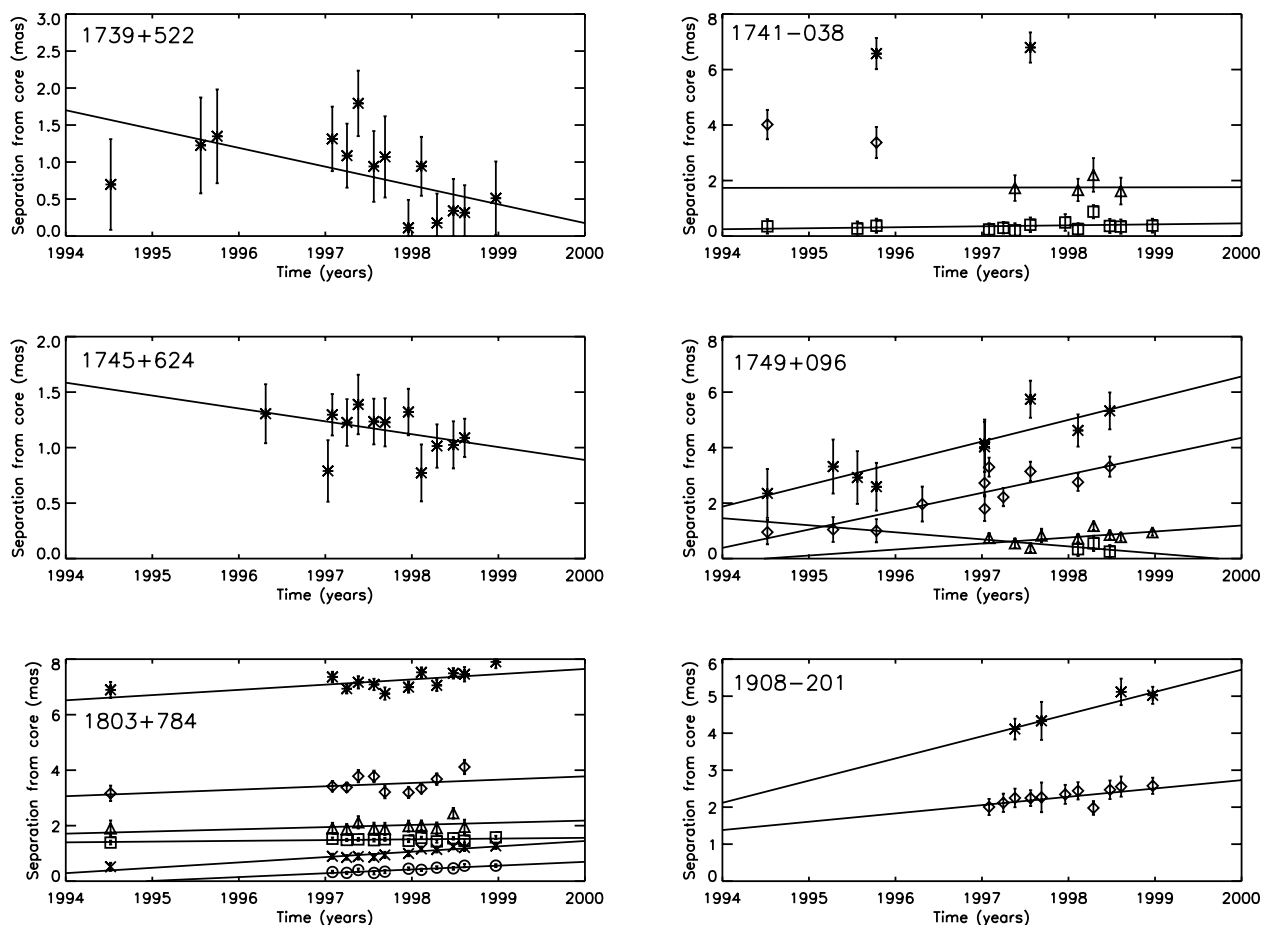
Fig. 2—*Continued*

samples should be observed at the same frequencies. K04 split the 2 cm survey sources into two groups based on their EGRET detection or nondetection, and found that the apparent speed distributions of the two groups differed, but at a relatively low significance level of 90%. Here we perform a similar calculation for the sources in the RRFID kinematic survey. Of the 54 sources represented in the fastest-component histogram in Figure 5, 16 are EGRET detections according to the analyses by Mattox et al. (2001) and Sowards-Emmerd et al. (2003). Figure 7 shows the histogram in Figure 5 separated according to EGRET detection, with the top panel representing the EGRET detections and the bottom panel the nondetections. There is no significant statistical difference between the means of the two distributions shown in Figure 7. A K-S test also shows no significant difference between the fastest apparent speeds of the EGRET and non-EGRET sources. However, neither the 2 cm survey nor the RRFID survey represents a complete sample of gamma-ray sources, so both will be biased toward those EGRET sources with higher radio fluxes. The issue is likely to remain open until large flux-limited samples in both wave bands are studied with VLBI with identical experimental setups. Such studies will be significantly improved by the coming launch of *GLAST*, which should greatly increase the size of gamma-ray-selected blazar samples.

5. SOURCE-BY-SOURCE COMPARISON TO 2 cm SURVEY RESULTS

As discussed in § 3 the 2 cm survey observations described by K04 and the RRFID kinematic survey observations described here are nearly matched in angular resolution and sensitivity. Of the 77 sources included in Table 4, 36, or about half, also have measured apparent speeds published by K04 from the 2 cm survey data. This provides a unique opportunity to compare the results from the two surveys for the common sources, in order to see if the standard procedure of VLBI model fitting, component identification, and linear fitting yields reproducible results for the apparent speeds when the same sources are analyzed using different data sets by different groups. To aid in this comparison, all kinematic results in this paper were produced "blind" with respect to the 2 cm survey results, and the comparisons in this section were not made until after the kinematic results in § 4.1 had been finalized. We note that for some of the sources there are also numerous other published multiepoch VLBI results, but since those are typically over different time ranges or at different resolutions, we restrict the source-by-source comparison in this section to a comparison between results from this paper and those by K04.

Figure 8 shows the source-by-source comparison of the model-fit component positions, component identifications, and fitted apparent speeds for the 36 common sources in the RRFID kinematic survey and the 2 cm survey. The data and fits plotted in black in Figure 8 are the RRFID results transposed from Figure 2. The data and fits plotted in red in Figure 8 are the 2 cm survey results from Figure 1 of K04. Note first that there are many very nice cases of agreement between the two surveys: we point out the results for 1128+385 and 1308+326 as specific examples where the independent models from the two surveys are so
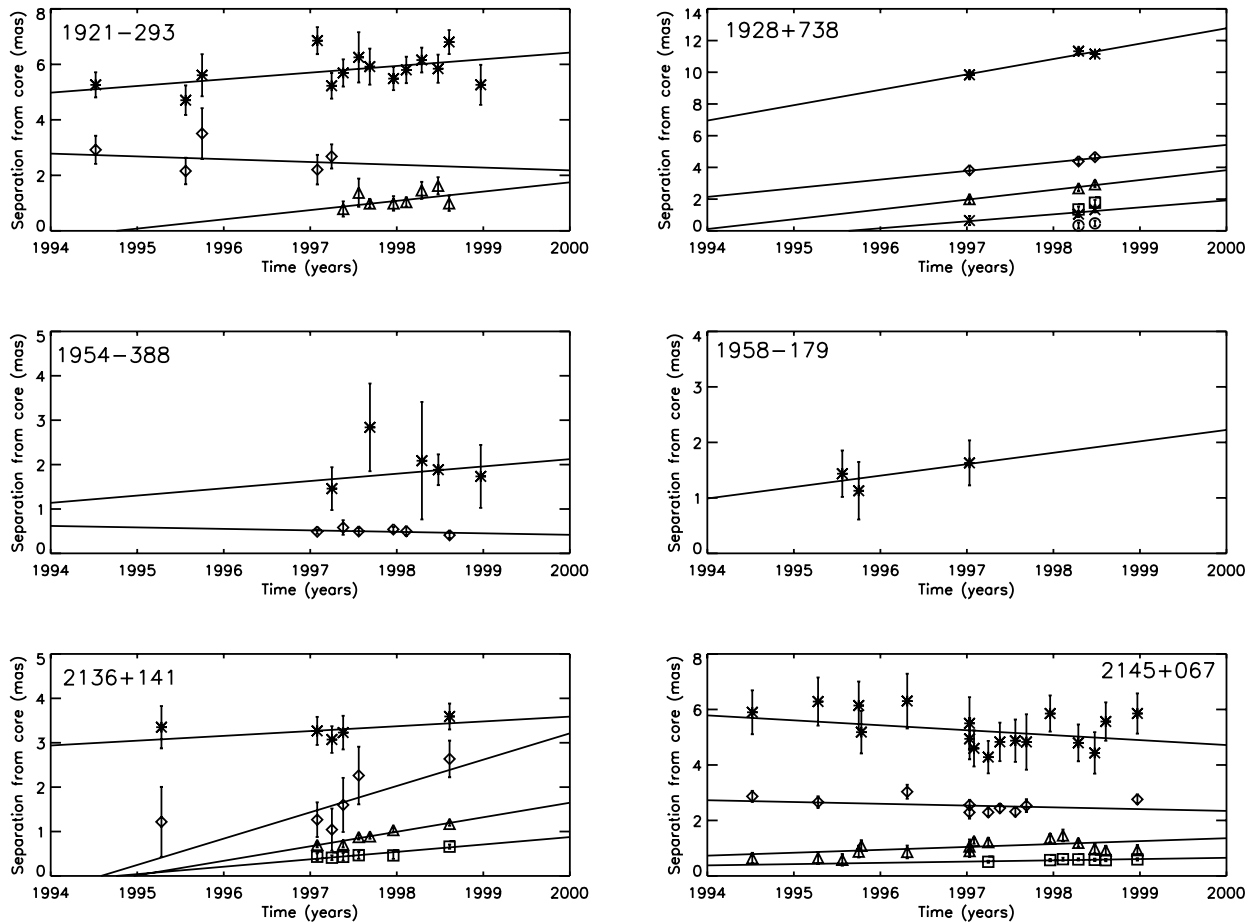
Fig. 2—*Continued*

close to each other on Figure 8 as to be nearly indistinguishable. However, there are other cases where the component identifications and measured apparent speeds are quite different; this issue is discussed in more detail below. There is no systematic detection of a consistent frequency-dependent separation of components from the cores in Figure 8; such frequency-dependent separation would be expected if sources have optically thick surfaces ("cores") at 8 and 15 GHz that are a significant distance apart. In most cases where the identification schemes agree, the separations at the two frequencies are the same within the errors, as in the two sources mentioned specifically above. We do note two cases of apparent frequency-dependent separation: in 2234+282, where the single component is about 0.5 mas farther from the core at 15 GHz, and in 0119+041, where the single component is about 0.2 mas closer to the core at 15 GHz (opposite the usual expected sense for frequency-dependent separation). In any event, any such frequency-dependent separations would not affect the apparent speed measurements, but only the estimated epoch of ejection from the core.

In these 36 sources, there are 66 components from the RRFID kinematic survey that can, in at least one epoch, be matched with a corresponding component from the same source from K04. From these 66 components, we list the 40 components (from 28 sources) with "good" or "excellent" quality codes in *both* surveys, together with their measured proper motions, in Table 6 (comparing proper motions rather than speeds avoids the issue of the slightly different cosmologies assumed by the two surveys). In a number of sources, different component identification schemes

were used for a given source in the two surveys, making the identification of which component from Table 4 "matches" which component from K04 problematic (the problem being that what is identified as a single component in one survey may have been identified as different components at different times in the other survey). In these cases the correspondence was made using the best-matching component pairs from the two data sets during the time period 1997–1998, when the RRFID observations are the most densely sampled.

The measured proper motions from this paper are plotted versus the corresponding proper motions from the 2 cm survey in Figure 9, using the 40 components from Table 6. The proper motions from the two surveys show a correlation with high significance (linear correlation coefficient of 0.81); however, this correlation is mainly due to the similar measurements for the proper motions of three components in BL Lac, which lie in the upper right corner of the figure. If those three components are excluded, then there is no statistically significant correlation between the proper motions measured by the two surveys. This lack of correlation is caused by the presence of a non-negligible subset of components with systematic differences between their proper motion measurements in the two surveys—this subset of components is identified and discussed in detail below. If that subset of 12 components is removed from Figure 9, then a correlation with high significance is recovered, even when the three components of BL Lac are excluded (linear correlation coefficient of 0.76).

We evaluated the agreement between the two surveys on a component-by-component basis by computing the significance
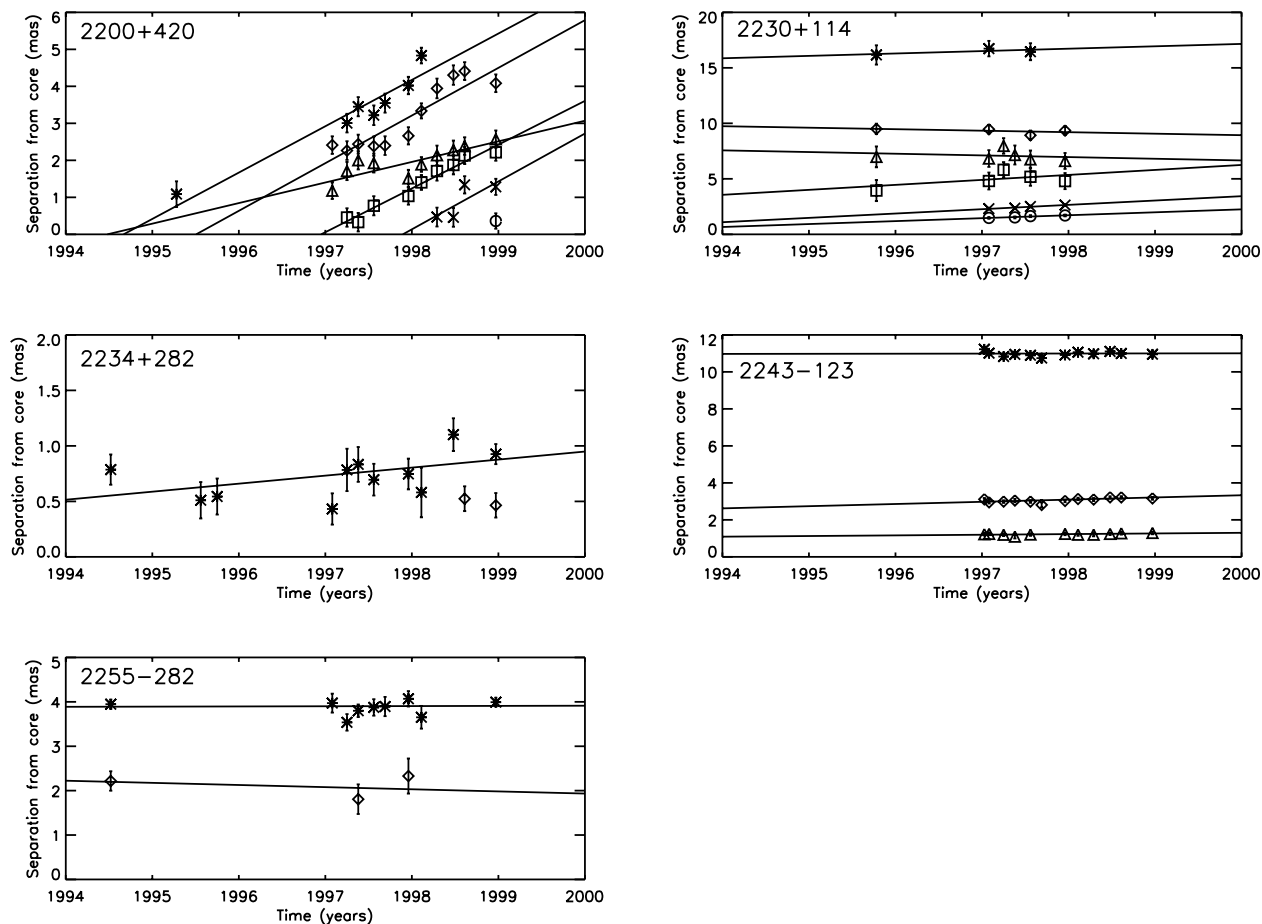
Fig. 2—*Continued*

of the difference in the two proper motion measurements for the matching components; this significance is tabulated for each component in Table 6. The significance of the difference in the two proper motions was computed from the probability associated with the reduced χ^2, computed from the fit of the two proper motions to their weighted average. For 12 of the 40 entries in Table 6 (or about 25% of the entries), the calculated significance exceeds 2.6 σ, corresponding to a probability $p < 0.01$ that the two proper motions are independent measurements of the same proper motion (these significances are marked with asterisks in Table 6). For these 12 components at least, there are some systematic errors in the interpretation of the VLBI data that are having an effect. Differences for the remaining 28 components follow approximately the expected normal distribution, as shown in Figure 10. In the rest of this section, we attempt to identify the types of systematic errors that have affected the 12 outlying components. We have classified these systematic errors into three types, and a code is given for the type of error or errors applicable to each of these 12 components in the last column of Table 6. Below we discuss these types of errors in detail, with specific examples of each:

Model-fit differences.—In the majority of cases where the RRFID kinematic survey and the 2 cm survey have data on the same source at nearly the same epoch, the fitted positions of the model components agree between the two surveys. However, in a small set of cases there is significant disagreement. For ex-

ample, in the 1995 epochs for 0003−066 in Figure 8, K04 measured the outermost component to be about 1 mas farther from the core, and they measure an extra component in between the two components measured by this paper. (At later epochs for this same source, e.g., 1998, the two surveys get nearly identical results.) Similar cases are indicated by the "MF" code in the final column of Table 6. It is interesting to note that the three sources that are noted as having different fitted component positions between the two surveys (0003−066, 0727−115, and 0823+033) are also among the 10% of sources mentioned in § 3.3 for which we obtain significantly different component positions from those obtained from the RRFID data by Fey et al. (1996) and Fey & Charlot (1997, 2000). If the corresponding fits from those references are added to Figure 8 for these sources, then they represent a third possible deconvolution of the source structure that does not agree with the other two. In these cases, the source structure is apparently ambiguous, and the deconvolution obtained is apparently quite sensitive to the data set and to the details of the model-fitting approach used.

Time baseline differences.—In some sources, the RRFID kinematic survey and the 2 cm survey obtain similar model-fit positions at epochs when both surveys have data, but positions measured at other times when only one of the two surveys has data cause differences in the apparent speed measurements. The second component in 2243−123 is an example of this. The first measurement of the position of this component by K04 in 1995 lies considerably below the extrapolation of the RRFID fit, as

TABLE 4
APPARENT COMPONENT SPEEDS

Source	Component	μ (mas yr^{-1})	β_{app}	ξ[a]	Distinct Component[b]	Quality Code[c]	2 cm Survey[d]
0003−066	1	0.308 ± 0.091	6.6 ± 2.0	2	Y	G	Y
	2	0.524 ± 0.124	11.3 ± 2.7	2	Y	G	
	3	−0.020 ± 0.029	−0.4 ± 0.6	4	Y	E	
0014+813	1	−0.083 ± 0.050	−8.9 ± 5.4	3	N	G	N
0059+581	1	−0.071 ± 0.067	−2.6 ± 2.5	2	Y	E	N
	2	0.106 ± 0.034	4.0 ± 1.2	3	N	G	
	3	−0.002 ± 0.022	−0.1 ± 0.8	4	N	G	
	4	0.025 ± 0.103	0.9 ± 3.8	3	N	F	
0104−408	1	−0.694 ± 0.883	−23.7 ± 30.2	1	N	P	N
0111+021........................	1	0.006 ± 0.238	0.0 ± 0.7	2	Y	P	N
	2	−0.074 ± 0.056	−0.2 ± 0.2	4	Y	E	
	3	0.008 ± 0.029	0.0 ± 0.1	5	N	G	
0119+041	1	0.013 ± 0.018	0.5 ± 0.7	4	N	G	Y
0119+115........................	1	0.050 ± 0.049	1.7 ± 1.7	4	N	G	N
	2	−0.018 ± 0.075	−0.6 ± 2.5	3	N	G	
0133+476	1	−0.052 ± 0.093	−2.5 ± 4.4	2	Y	G	Y
	2	0.366 ± 0.047	17.2 ± 2.2	4	N	G	
	3	0.385 ± 0.081	18.0 ± 3.8	4	N	F	
0146+056	1	0.068 ± 0.098	6.2 ± 8.9	3	N	F	N
0201+113	1	0.103 ± 0.055	11.4 ± 6.1	3	N	G	N
	2	0.047 ± 0.037	5.2 ± 4.2	4	N	G	
0202+149	1	−0.053 ± 0.034	−1.3 ± 0.8	4	Y	E	Y
	2	0.062 ± 0.033	1.5 ± 0.8	4	N	G	
0229+131	1	−0.202 ± 0.135	−17.1 ± 11.4	3	N	F	N
	2	0.156 ± 0.090	13.2 ± 7.6	2	Y	G	
	3	0.384 ± 0.107	32.5 ± 9.1	2	N	F	
	4	−0.066 ± 0.067	−5.6 ± 5.7	4	N	G	
0234+285	1	0.137 ± 0.091	8.3 ± 5.5	2	Y	G	Y
	2	0.159 ± 0.023	9.6 ± 1.4	4	Y	E	
	3	0.068 ± 0.103	4.1 ± 6.2	2	N	F	
	4	0.013 ± 0.388	0.8 ± 23.5	3	N	P	
0336−019	1	0.436 ± 0.219	20.3 ± 10.2	2	Y	P	Y
	2	0.151 ± 0.093	7.0 ± 4.4	2	N	F	
	3	0.183 ± 0.037	8.5 ± 1.7	3	Y	E	
0402−362	1	0.386 ± 0.152	26.0 ± 10.2	3	Y	P	N
	2	0.032 ± 0.083	2.2 ± 5.6	4	N	F	
0454−234	1	0.116 ± 0.130	6.2 ± 6.9	2	N	F	N
0458−020	1	−0.558 ± 0.232	−50.1 ± 20.8	2	Y	P	Y
	2	−0.019 ± 0.044	−1.7 ± 3.9	4	Y	E	
0528+134	1	−0.166 ± 0.111	−14.1 ± 9.4	2	Y	G	Y
	2	−0.034 ± 0.050	−2.9 ± 4.2	3	N	G	
	3	0.016 ± 0.023	1.3 ± 1.9	4	N	G	
0537−441	1	1.109 ± 0.478	53.7 ± 23.1	1	N	P	N
0552+398	1	−0.003 ± 0.006	−0.2 ± 0.6	5	N	G	N
0642+449	1	0.172 ± 0.112	18.6 ± 12.2	2	Y	G	Y
	2	0.037 ± 0.014	4.0 ± 1.5	5	N	G	
0727−115........................	1	−0.035 ± 0.044	−2.5 ± 3.2	3	Y	E	Y
	2	0.054 ± 0.065	3.9 ± 4.7	3	N	G	
	3	0.011 ± 0.062	0.8 ± 4.5	5	N	F	
0742+103	1	0.078 ± 0.115	7.5 ± 11.1	3	N	F	Y
	2	−0.071 ± 0.078	−6.8 ± 7.5	3	N	G	
	3	−0.037 ± 0.018	−3.5 ± 1.8	5	N	G	
0804+499	1	0.195 ± 0.080	13.2 ± 5.4	2	Y	E	Y
	2	−0.228 ± 0.257	−15.5 ± 17.4	2	N	P	
0805+410	3	−0.073 ± 0.322	−4.9 ± 21.7	2	N	P	N
0823+033	1	−0.016 ± 0.056	−0.5 ± 1.7	3	Y	E	Y
	2	0.019 ± 0.027	0.6 ± 0.8	4	N	G	
0851+202	1	−0.039 ± 0.109	−0.7 ± 2.1	1	N	F	Y
	2	0.296 ± 0.082	5.7 ± 1.6	4	N	P	
	3	0.386 ± 0.043	7.4 ± 0.8	3	N	G	
	4	−0.031 ± 0.059	−0.6 ± 1.1	4	N	G	
0919−260	1	0.565 ± 0.125	50.8 ± 11.3	2	N	F	N
	2	0.038 ± 0.036	3.4 ± 3.2	3	N	G	
0920−397	1	0.867 ± 0.436	29.9 ± 15.1	2	N	P	N

TABLE 4—*Continued*

Source	Component	μ (mas yr^{-1})	β_{app}	ξ[a]	Distinct Component[b]	Quality Code[c]	2 cm Survey[d]
0923+392.........................	1	0.122 ± 0.119	4.8 ± 4.7	2	N	F	Y
	2	0.053 ± 0.070	2.1 ± 2.8	2	Y	E	
	3	0.044 ± 0.107	1.7 ± 4.2	2	N	F	
0953+254.........................	1	-0.169 ± 0.304	-6.8 ± 12.3	2	N	P	Y
	2	0.163 ± 0.189	6.6 ± 7.6	3	N	P	
0955+476.........................	1	0.268 ± 0.090	21.5 ± 7.2	2	N	F	N
	2	0.105 ± 0.143	8.4 ± 11.4	2	N	F	
1004+141.........................	1	-0.060 ± 0.034	-5.8 ± 3.3	4	Y	E	N
	2	-0.542 ± 0.260	-53.0 ± 25.4	2	N	P	
	3	-0.081 ± 0.118	-8.0 ± 11.5	2	N	F	
	4	0.004 ± 0.054	0.4 ± 5.3	3	N	G	
1022+194.........................	3	0.176 ± 0.059	8.0 ± 2.7	3	Y	G	N
	4	0.150 ± 0.061	6.8 ± 2.8	3	N	F	
1034−293.........................	1	1.457 ± 0.292	28.5 ± 5.7	2	N	P	N
	2	1.215 ± 0.187	23.7 ± 3.6	4	N	G	
1044+719.........................	1	0.160 ± 0.091	9.4 ± 5.3	2	N	F	N
1101+384.........................	1	-0.272 ± 0.235	-0.5 ± 0.5	2	N	P	Y
	2	0.000 ± 0.041	0.0 ± 0.1	4	N	G	
	3	-0.067 ± 0.068	-0.1 ± 0.1	3	N	G	
1124−186.........................	1	0.033 ± 0.539	1.8 ± 29.5	2	N	P	N
	2	0.072 ± 0.098	4.0 ± 5.4	3	N	F	
1128+385.........................	1	0.001 ± 0.038	0.1 ± 2.9	3	N	G	Y
	2	0.014 ± 0.016	1.1 ± 1.2	5	N	G	
1144−379.........................	1	-0.195 ± 0.140	-10.6 ± 7.7	3	N	F	N
1145−071.........................	1	0.059 ± 0.012	3.8 ± 0.8	5	Y	E	N
1156+295.........................	1	-0.386 ± 0.274	-15.9 ± 11.3	1	N	P	Y
	2	0.452 ± 0.185	18.6 ± 7.6	1	Y	P	
	3	0.155 ± 0.094	6.4 ± 3.9	2	N	F	
1219+044.........................	1	0.064 ± 0.038	3.3 ± 2.0	4	N	G	N
1228+126.........................	1	0.241 ± 0.209	0.07 ± 0.06	2	N	P	Y
	2	0.251 ± 0.095	0.07 ± 0.03	2	N	F	
	3	0.051 ± 0.066	0.01 ± 0.02	3	N	G	
1253−055.........................	1	0.181 ± 0.046	5.7 ± 1.5	4	Y	G	Y
	2	0.188 ± 0.120	6.0 ± 3.8	3	N	P	
	3	-0.027 ± 0.120	-0.9 ± 3.8	3	N	P	
1255−316.........................	2	-0.848 ± 0.699	-69.1 ± 56.9	3	Y	P	N
	3	0.248 ± 0.561	20.2 ± 45.7	3	Y	P	
1308+326.........................	1	0.343 ± 0.014	18.0 ± 0.8	5	N	G	Y
1313−333.........................	1	0.376 ± 0.083	22.7 ± 5.0	3	N	F	N
	2	0.156 ± 0.056	9.5 ± 3.4	3	N	G	
1334−127.........................	1	0.011 ± 0.038	0.4 ± 1.2	5	Y	E	Y
	2	0.276 ± 0.080	8.8 ± 2.6	4	N	G	
1351−018.........................	1	0.278 ± 0.250	31.4 ± 28.1	3	N	P	N
1418+546.........................	1	0.055 ± 0.079	0.5 ± 0.8	3	Y	E	N
	2	-0.008 ± 0.079	-0.1 ± 0.8	3	Y	E	
	3	0.027 ± 0.198	0.3 ± 1.9	2	N	P	
1424−418.........................	1	-0.001 ± 0.887	-0.1 ± 62.6	2	N	P	N
1451−375.........................	1	-0.533 ± 1.972	-10.5 ± 38.7	1	N	P	N
	2	-0.011 ± 0.377	-0.2 ± 7.4	2	N	P	
1514−241.........................	1	3.593 ± 0.746	11.6 ± 2.4	1	N	P	N
	2	0.957 ± 0.360	3.1 ± 1.2	2	N	P	
	3	0.337 ± 0.337	1.1 ± 1.1	2	N	P	
	4	0.231 ± 0.192	0.7 ± 0.6	3	N	P	
1606+106.........................	1	-0.136 ± 0.070	-8.3 ± 4.3	3	N	G	Y
	2	0.019 ± 0.063	1.1 ± 3.8	3	N	G	
	3	0.089 ± 0.049	5.5 ± 3.0	3	N	G	
	4	-0.092 ± 0.032	-5.6 ± 2.0	4	N	G	
1611+343.........................	1	0.029 ± 0.022	1.9 ± 1.5	4	N	G	Y
	2	0.063 ± 0.022	4.2 ± 1.5	4	Y	E	
	3	0.027 ± 0.073	1.8 ± 4.9	3	N	G	
1622−253.........................	1	0.229 ± 0.138	10.0 ± 6.0	2	N	F	N
	2	-0.130 ± 0.274	-5.7 ± 12.0	2	N	P	
1638+398.........................	1	-0.022 ± 0.077	-1.7 ± 5.8	2	N	G	N

TABLE 4—*Continued*

Source	Component	μ (mas yr^{-1})	β_{app}	ξ[a]	Distinct Component[b]	Quality Code[c]	2 cm Survey[d]
1652+398	1	-0.090 ± 0.111	-0.2 ± 0.2	2	Y	F	Y
	2	0.162 ± 0.113	0.4 ± 0.3	2	Y	F	
	3	0.090 ± 0.059	0.2 ± 0.1	3	Y	G	
	4	0.009 ± 0.030	0.0 ± 0.1	4	N	F	
1726+455	1	0.202 ± 0.045	8.2 ± 1.8	3	Y	E	N
	2	0.025 ± 0.127	1.0 ± 5.2	3	N	F	
1739+522	1	-0.254 ± 0.119	-16.8 ± 7.9	1	N	F	N
1741−038	3	0.004 ± 0.528	0.2 ± 28.9	2	N	P	N
	4	0.035 ± 0.056	1.9 ± 3.1	3	N	G	
1745+624	1	-0.116 ± 0.098	-13.3 ± 11.2	2	N	F	N
1749+096	1	0.782 ± 0.202	15.7 ± 4.1	1	N	P	Y
	2	0.661 ± 0.107	13.3 ± 2.1	2	N	G	
	3	0.217 ± 0.087	4.4 ± 1.7	3	N	F	
	4	-0.254 ± 0.936	-5.1 ± 18.8	2	N	P	
1803+784	1	0.189 ± 0.068	7.3 ± 2.6	2	N	G	Y
	2	0.119 ± 0.076	4.6 ± 3.0	2	N	G	
	3	0.078 ± 0.073	3.0 ± 2.8	2	N	G	
	4	0.027 ± 0.017	1.0 ± 0.7	4	Y	E	
	5	0.193 ± 0.034	7.5 ± 1.3	3	N	G	
	6	0.137 ± 0.027	5.3 ± 1.0	4	N	G	
1908−201	1	0.600 ± 0.217	34.3 ± 12.4	2	N	P	N
	2	0.225 ± 0.121	12.9 ± 6.9	3	Y	G	
1921−293	1	0.241 ± 0.110	5.3 ± 2.4	2	Y	G	Y
	2	-0.101 ± 0.216	-2.2 ± 4.7	2	N	P	
	3	0.333 ± 0.234	7.3 ± 5.1	3	N	P	
1928+738	1	0.971 ± 0.217	18.4 ± 4.1	2	Y	P	Y
	2	0.547 ± 0.223	10.4 ± 4.2	2	Y	P	
	3	0.619 ± 0.216	11.7 ± 4.1	2	Y	P	
	5	0.439 ± 0.229	8.3 ± 4.3	2	N	P	
1954−388	1	0.164 ± 0.410	6.0 ± 15.0	2	N	P	N
	2	-0.033 ± 0.051	-1.2 ± 1.8	5	N	G	
1958−179	1	0.206 ± 0.372	7.7 ± 13.9	2	N	P	N
2136+141	1	0.108 ± 0.162	10.0 ± 15.0	2	Y	P	Y
	2	0.593 ± 0.246	54.9 ± 22.8	1	N	P	
	3	0.327 ± 0.041	30.3 ± 3.8	4	N	G	
	4	0.167 ± 0.044	15.5 ± 4.1	4	N	G	
2145+067	1	-0.178 ± 0.156	-9.3 ± 8.2	1	N	P	Y
	2	-0.064 ± 0.051	-3.4 ± 2.7	3	N	G	
	3	0.105 ± 0.036	5.5 ± 1.9	3	N	G	
	4	0.046 ± 0.030	2.4 ± 1.6	5	N	G	
2200+420	1	1.253 ± 0.136	5.7 ± 0.6	2	N	G	Y
	2	1.288 ± 0.128	5.8 ± 0.6	2	Y	E	
	3	0.556 ± 0.126	2.5 ± 0.6	2	N	F	
	4	1.183 ± 0.146	5.4 ± 0.7	2	Y	E	
	5	1.294 ± 0.469	5.9 ± 2.1	2	N	P	
2230+114	1	0.215 ± 0.639	11.7 ± 34.6	1	N	P	Y
	2	-0.135 ± 0.264	-7.3 ± 14.3	2	N	P	
	3	-0.151 ± 0.525	-8.2 ± 28.5	1	Y	P	
	4	0.448 ± 0.533	24.3 ± 28.9	1	N	P	
	5	0.391 ± 0.139	21.1 ± 7.5	4	N	F	
	6	0.265 ± 0.130	14.3 ± 7.0	4	Y	G	
2234+282	1	0.072 ± 0.031	3.2 ± 1.4	3	N	G	Y
2243−123	1	0.006 ± 0.060	0.2 ± 2.2	4	Y	E	Y
	2	0.118 ± 0.033	4.3 ± 1.2	5	Y	E	
	3	0.035 ± 0.035	1.3 ± 1.3	5	N	G	
2255−282	1	0.004 ± 0.032	0.2 ± 1.6	4	Y	E	N
	2	-0.048 ± 0.108	-2.4 ± 5.4	3	N	P	

NOTE.—Table 4 is also available in machine-readable form in the electronic edition of the *Astronomical Journal*.

[a] Error bars on component positions were computed as a fraction $1/2^{\xi}$ of the beam size, where ξ was a function of the average flux of the component; see § 4.1.

[b] Whether or not the component is a distinct feature; Y = yes, N = no.

[c] Overall quality code; see text for definitions.

[d] Whether or not the source has an apparent speed measured from the 2 cm survey (K04); Y = yes, N = no.
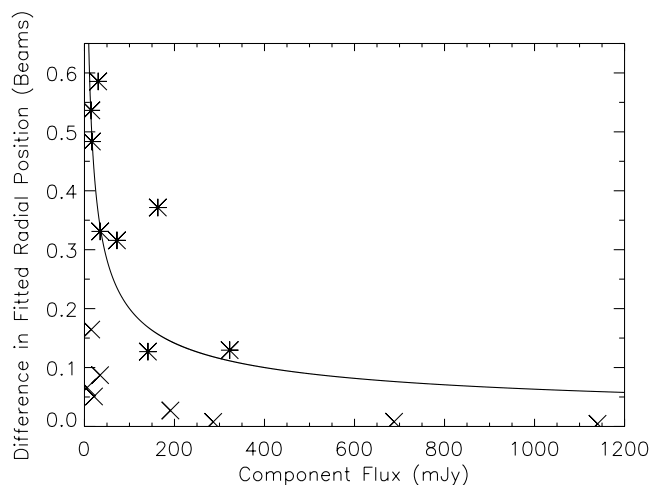
FIG. 3.—Difference in the model-fit radial positions of common components in the adjacent epoch pairs defined in § 4.1 vs. the component flux. The beam size is computed as the average of the radial beam size in the two epochs (projection of the beam onto a radial line at the component's position angle), and the flux is the average flux from the two epochs. The solid line shows an estimate of the upper envelope of this distribution, $\Delta r \approx 2S^{-1/2}$, where Δr is measured in beams and S is measured in millijanskys. The upper envelope was obtained by a fit to the eight points indicated by asterisks; the points falling considerably below the upper envelope are indicated by crosses.

if the component decelerated sometime during the years 1995–1997. In fact, if components do not accelerate or decelerate, then differences in the time baseline should have no affect on the apparent speed measurements (other than to reduce the random error), so we conclude that such components are most likely cases of apparent acceleration or deceleration of the radial motion. Such cases are indicated by the TB code in the final column of Table 6. There are additional examples of this, such as the inner component in 0202+149, that did not meet the criteria for inclusion in Table 6.

Different component identification schemes.—A subset of sources exists where both the 2 cm survey and the RRFID kinematic survey have measured similar positions for model-fit components at similar epochs, but where the components have been identified differently from epoch to epoch to yield different sets of "components" with different speeds. The source 1606+106 in Figure 8 provides an example of this. If one

FIG. 5.—Histogram of the fastest apparent component speed in each source, for the 54 sources represented in Fig. 4.
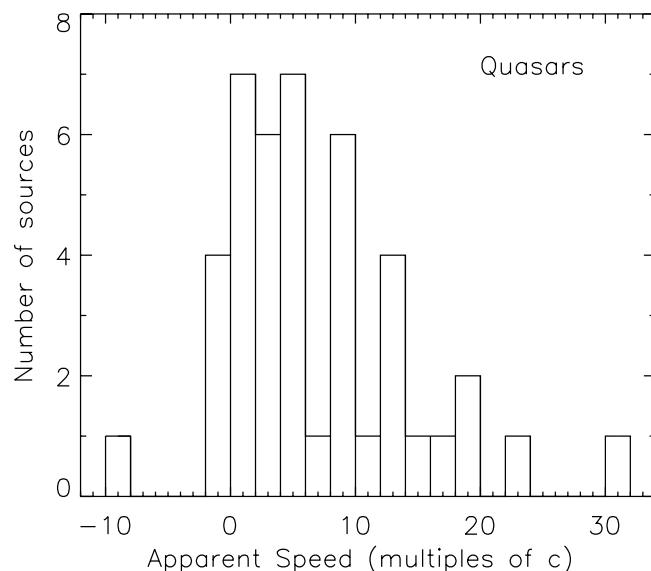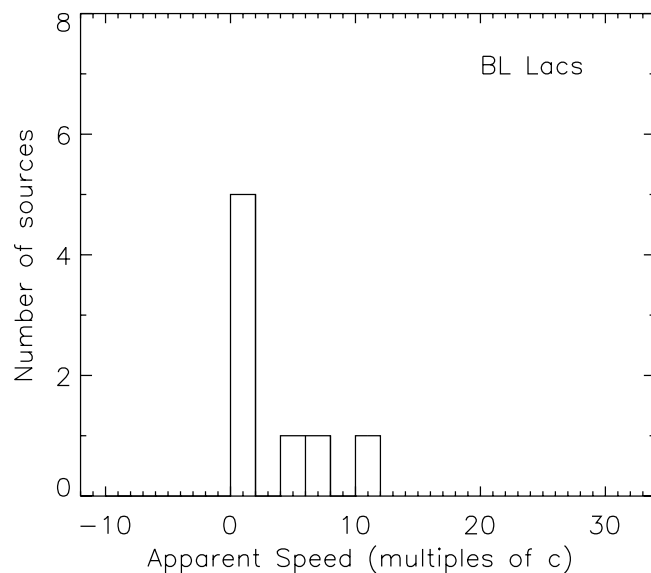
FIG. 6.—Histograms of the fastest apparent component speed in each source, for the 54 sources represented in Fig. 5, separated by optical type. The top panel shows the BL Lac objects (8 sources), and the bottom panel shows the quasars (43 sources). Three sources classified as galaxies are not shown.

FIG. 4.—Histogram of apparent component speeds for the 94 components in Table 4 that have a "good" or "excellent" quality code.

TABLE 5
NONRADIAL TRAJECTORIES

Source	Component	$\overline{\mathrm{P.A.}}$ [a] (deg)	ϕ [b] (deg)	β_{app} [c]	$|\overline{\mathrm{P.A.}} - \phi|$ (deg)
0234+285	C2	-13.5 ± 0.3	3.2 ± 5.0	10.2 ± 1.4	16.6 ± 5.0
0823+033	C2	26.4 ± 1.3	100.6 ± 20.9	2.4 ± 0.4	74.2 ± 21.0
1611+343	C1	163.5 ± 0.2	-117.2 ± 7.1	11.2 ± 1.1	79.3 ± 7.1
1622$-$253	C1	-11.0 ± 1.5	-66.9 ± 16.1	20.6 ± 3.2	55.9 ± 16.1
2136+141	C3	-104.3 ± 2.6	-151.3 ± 5.9	45.7 ± 6.5	47.0 ± 6.5
2200+420	C3	-167.9 ± 1.8	161.5 ± 9.1	3.0 ± 0.6	30.6 ± 9.3

[a] Average P.A. of the component.
[b] Fitted direction of motion of the component.
[c] Magnitude of the velocity vector of the component.
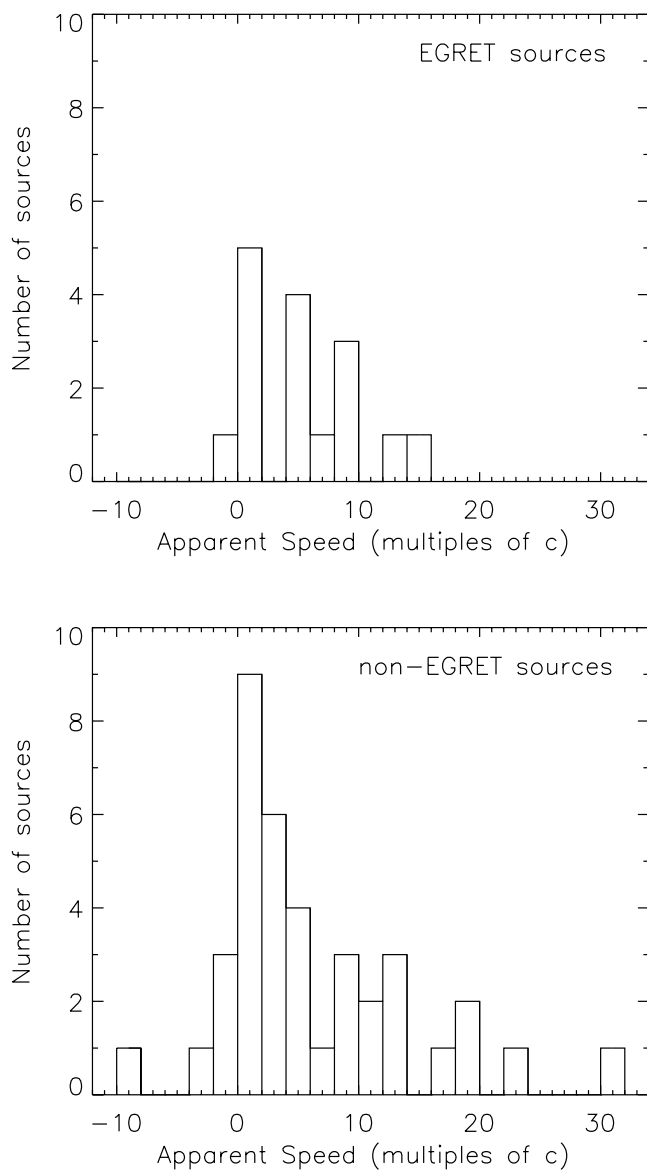
FIG. 7.—Histograms of the fastest apparent component speed in each source, for the 54 sources represented in Fig. 5, separated by EGRET detection status. EGRET sources from Mattox et al. (2001) and Sowards-Emmerd et al. (2003) are in the top panel (16 sources); sources not detected by EGRET are in the bottom panel (38 sources).

considers the data for component 3 in this source from the RRFID kinematic survey (black triangles in Fig. 8 and associated black line fit), then it can be seen that there is a matching 2 cm survey component in 1996 (identified as their component D), another in 1997 (identified as their component C), and another in 1999 (identified as their component B). This is typical of this general problem; one survey has interpreted the position data as a smaller number of more slowly moving components, while the other has interpreted them with a larger number of faster components. In these cases, it is the spacing of the epochs in time that is the major influence on component identification. For 1606+106, the dense spacing of the RRFID position data during 1997 and 1998 seems to preclude the faster interpretation of K04. Four other sources where differing component identification schemes have yielded significantly different apparent speed measurements are indicated by the "ID" code in the final column of Table 6. None of these components were recorded as "distinct features" in *both* surveys, so seeing a component as a distinct rather than a blended feature on the images evidently helps prevent ambiguities in component identification. In addition, there are five other sources where components were identified differently by the two surveys, but where the motions did not meet the criteria for inclusion in Table 6, or where this did not result in apparent speed differences at the cutoff significance level specified for the analysis in this section. In total, different component identification schemes were used for 10 of the 36 common sources. For those discrepant sources that have densely spaced RRFID observations during 1997 and 1998, we expect that the more densely spaced RRFID data should better resolve potential ambiguities in component identification.

Ambiguities in identifying VLBI components from epoch to epoch have long been discussed as a potential problem for multiepoch VLBI observations (see, for example, the discussion of this issue in the context of the CJF survey by Vermeulen et al. 2003). However, this is the first time that this issue has been quantitatively addressed using independently analyzed data sets for a sizable number of common sources. If the results from this paper can be extrapolated to similar multiepoch VLBI studies, then roughly 25% of the apparent speed measurements in the literature may not be repeatable, in the sense that other observers using a similar but independent set of VLBI observations may have reached different conclusions about the apparent speeds. Component identification should be considered more reliable for distinct features on the images and should also become more robust as the time density of epochs increases, because there are fewer consistent ways in which the
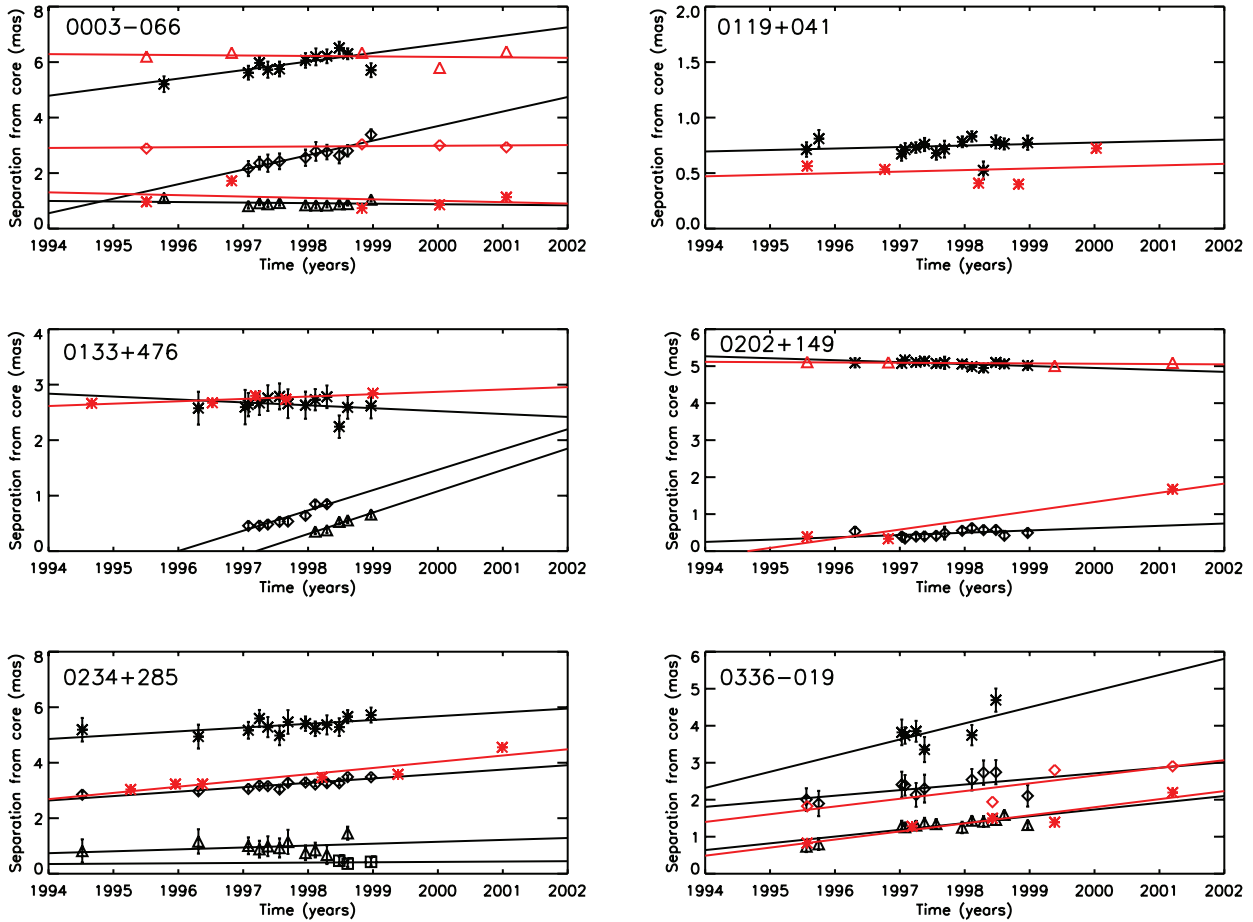
FIG. 8.—Comparison of model-fit component positions and fitted apparent speeds for the common sources in the RRFID kinematic survey and 2 cm surveys. The data and fits plotted in black are the results from this paper transposed from Fig. 2. The data and fits plotted in red are the 2 cm survey results from Fig. 1 of K04. For the RRFID data, component symbols are the same as those used in Fig. 2. For the 2 cm survey data, asterisks are used to represent component B, diamonds for component C, triangles for component D, squares for component E, and crosses for component F, as identified by K04.

FIG. 8—*Continued*

Fig. 8—*Continued*

F_{IG.} 8— *Continued*

Fig. 8—*Continued*

2384
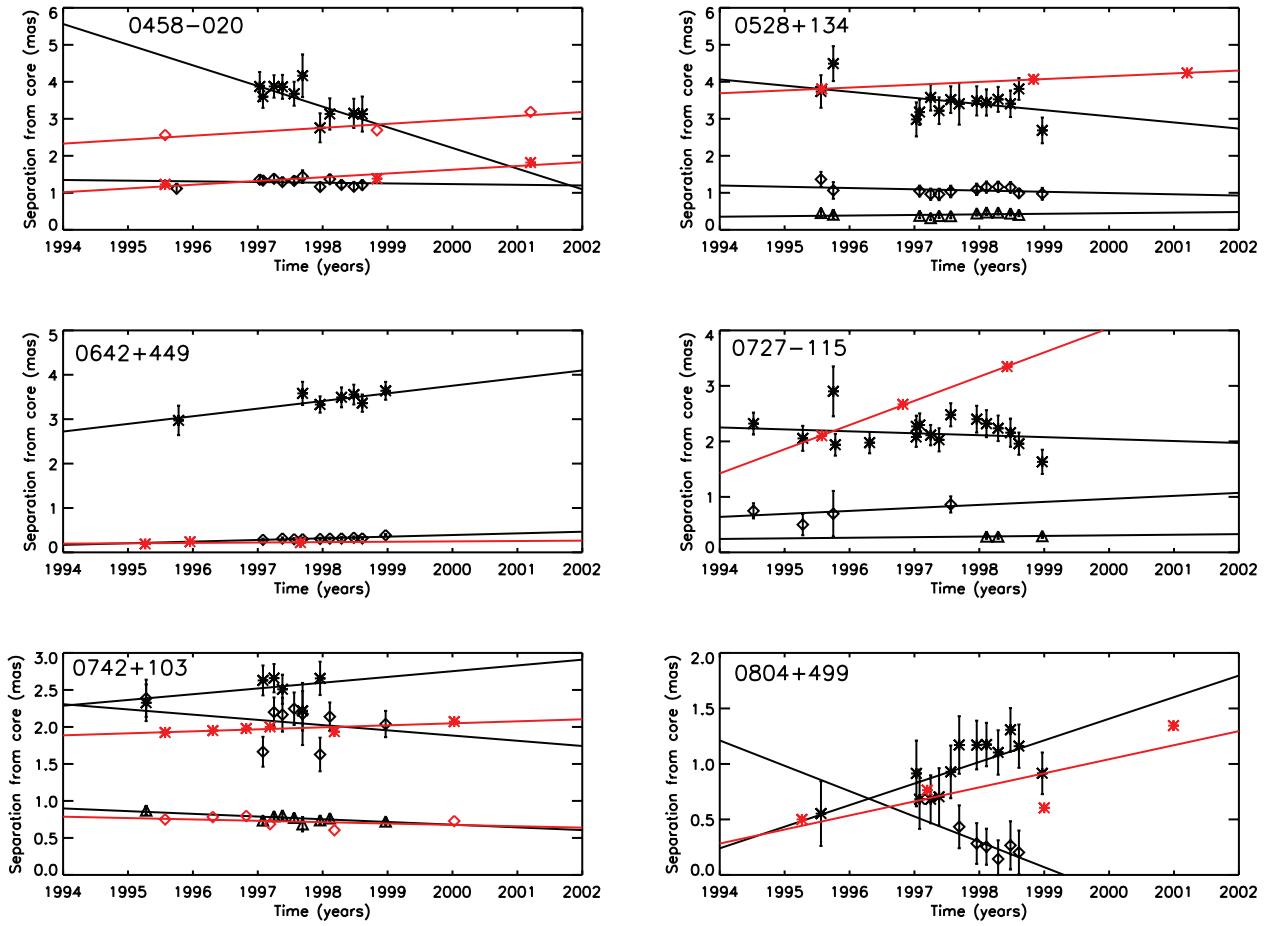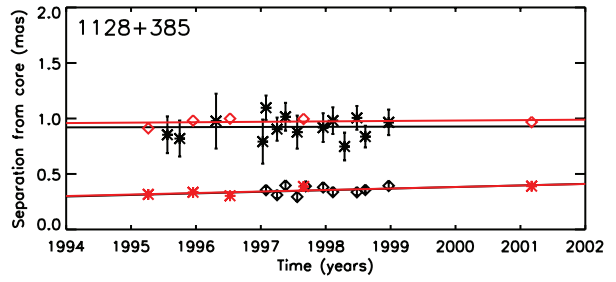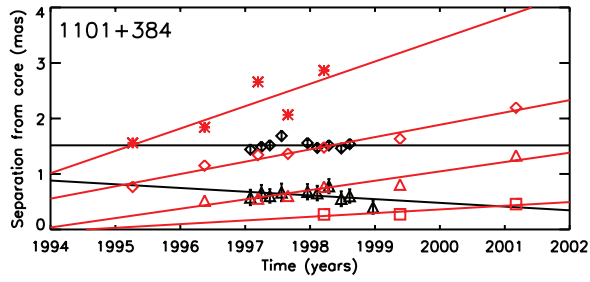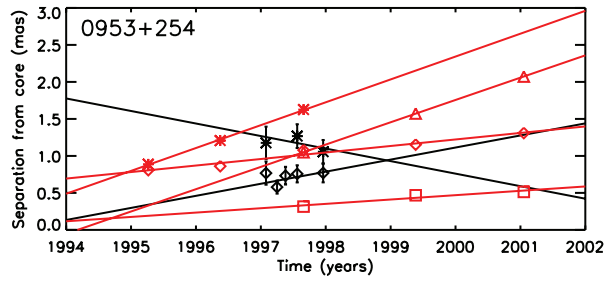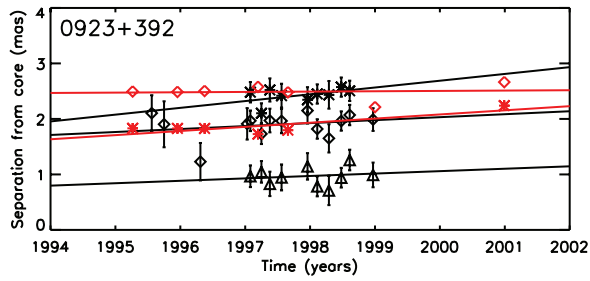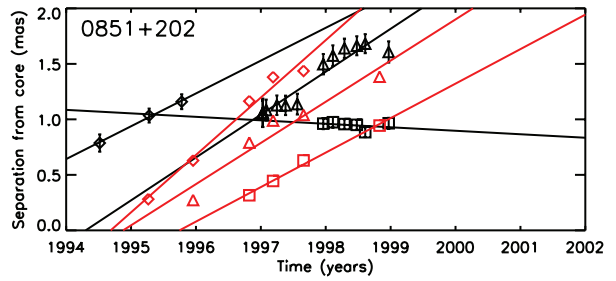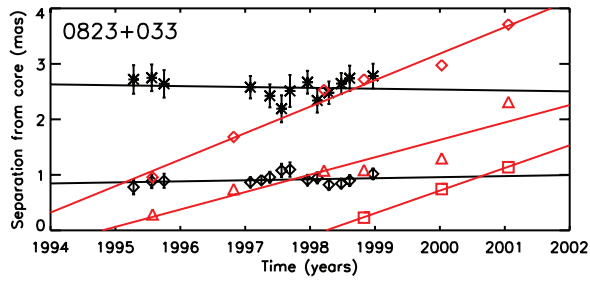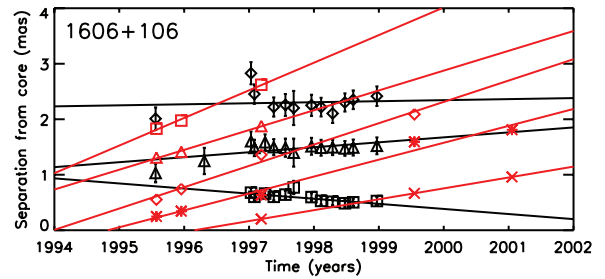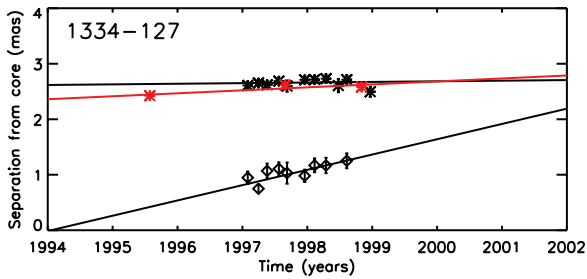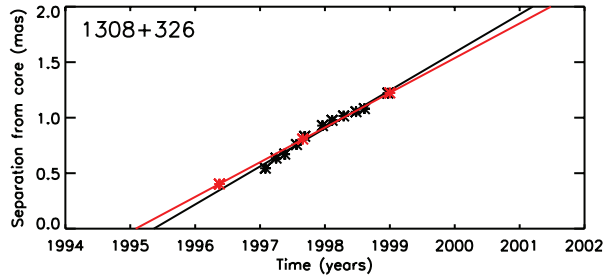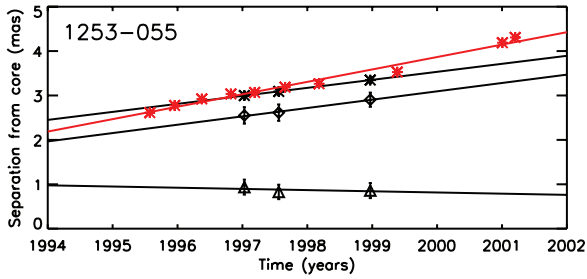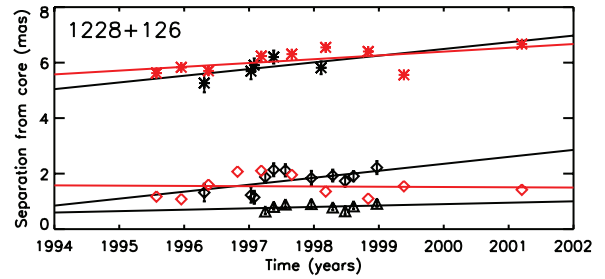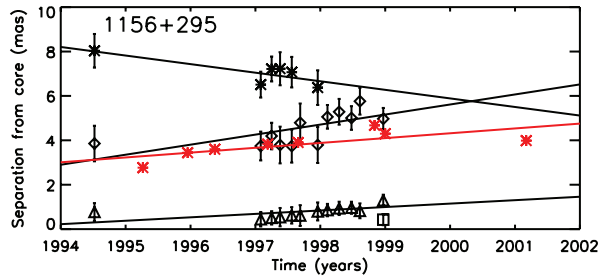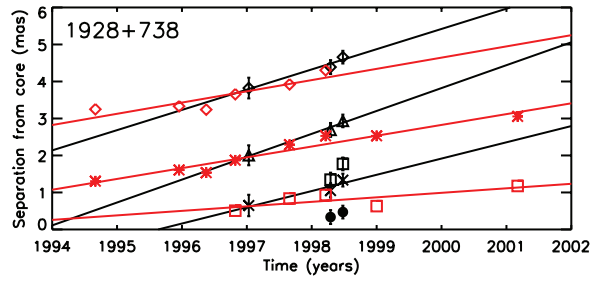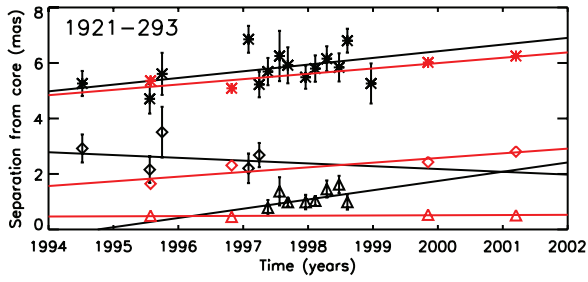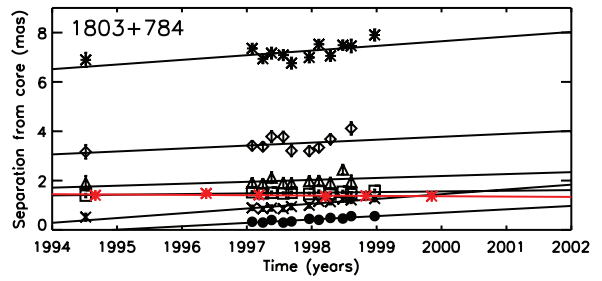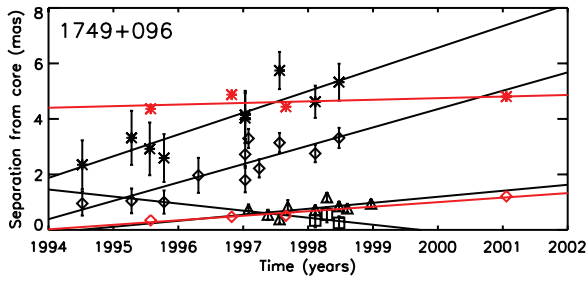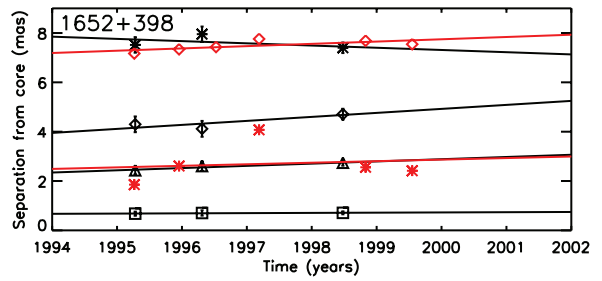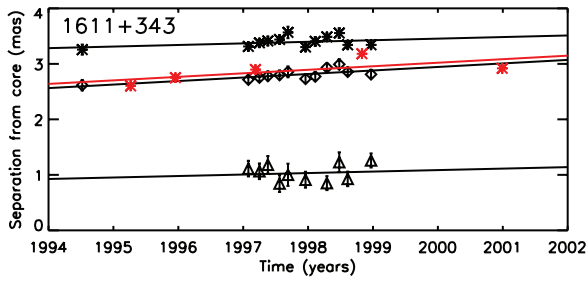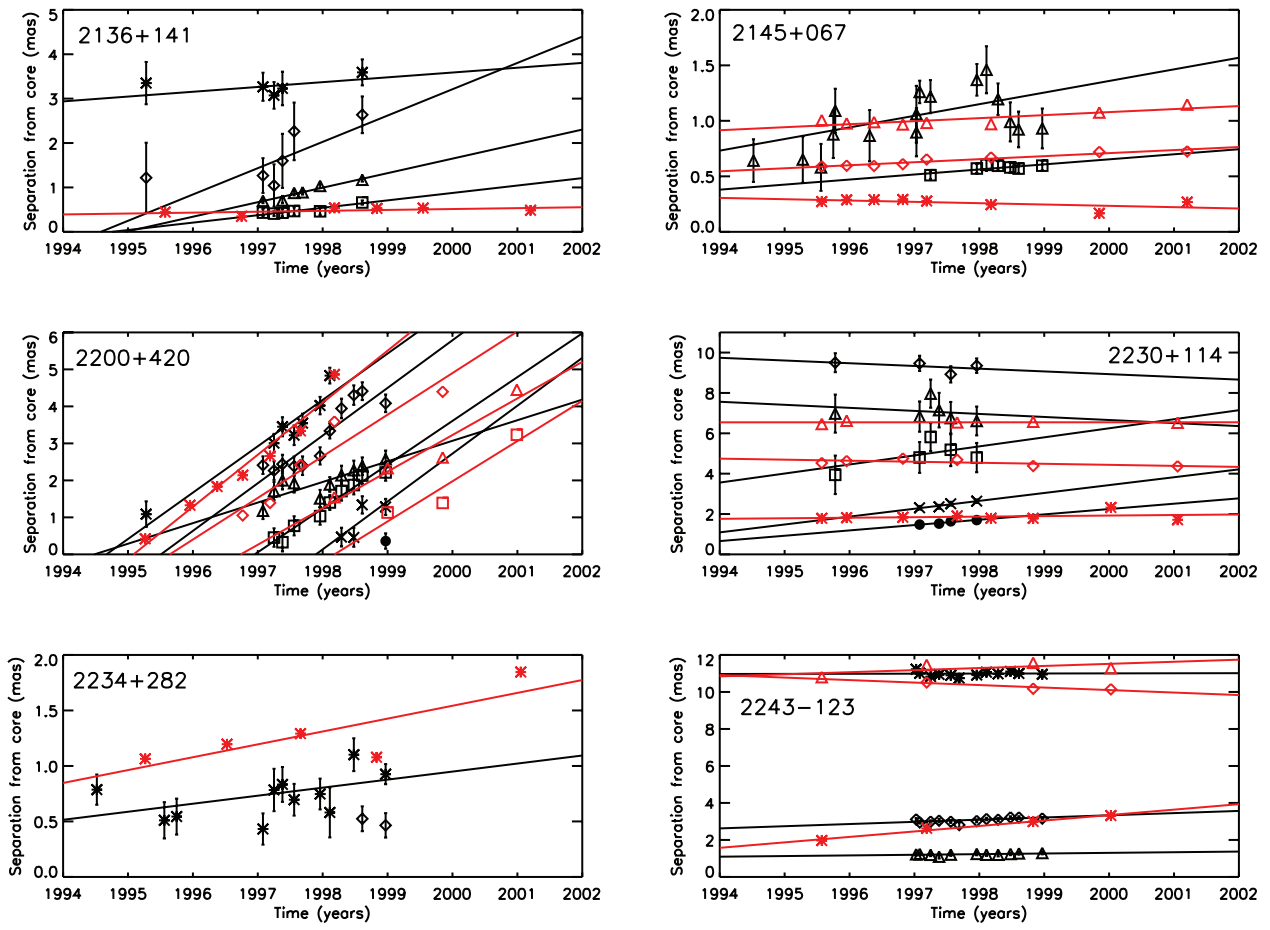
Fig. 8—*Continued*

TABLE 6
COMPARISON OF MEASURED PROPER MOTIONS FOR "GOOD" AND "EXCELLENT" COMPONENTS

Source	RRFID Component[a]	RRFID Proper Motion[a] (mas yr^{-1})	2 cm Component[b]	2 cm Proper Motion[b] (mas yr^{-1})	Difference in σ[c]	Cause of Disagreement[d]
0003−066	1	0.308 ± 0.091	D	−0.02 ± 0.06	3.0*	MF, TB
	2	0.524 ± 0.124	C	0.01 ± 0.02	4.1*	MF, TB
	3	−0.020 ± 0.029	B	−0.05 ± 0.09	0.3	
0119+041	1	0.013 ± 0.018	B	0.01 ± 0.04	0.1	
0133+476	1	−0.052 ± 0.093	B	0.04 ± 0.01	1.0	
0202+149	1	−0.053 ± 0.034	D	−0.01 ± 0.01	1.2	
0234+285	2	0.159 ± 0.023	B	0.23 ± 0.05	1.3	
0336−019	3	0.183 ± 0.037	B	0.22 ± 0.04	0.7	
0458−020	2	−0.019 ± 0.044	B	0.10 ± 0.04	2.0	
0528+134	1	−0.166 ± 0.111	B	0.077 ± 0.002	2.2	
0727−115............	1	−0.035 ± 0.044	B	0.44 ± 0.01	10.5*	MF
0742+103	2	−0.071 ± 0.078	B	0.03 ± 0.01	1.3	
	3	−0.037 ± 0.018	C	−0.02 ± 0.02	0.6	
0804+499	1	0.195 ± 0.080	B	0.13 ± 0.06	0.7	
0823+033	1	−0.016 ± 0.056	C	0.48 ± 0.04	7.2*	MF, ID
	2	0.019 ± 0.027	D	0.31 ± 0.06	4.4*	ID
0851+202	3	0.386 ± 0.043	D	0.37 ± 0.06	0.2	
	4	−0.031 ± 0.059	E	0.31 ± 0.02	5.5*	ID
0923+392	2	0.053 ± 0.070	B	0.07 ± 0.03	0.2	
1101+384	2	0.000 ± 0.041	C	0.22 ± 0.02	4.8*	ID
	3	−0.067 ± 0.068	D	0.17 ± 0.03	3.2*	ID
1128+385	1	0.001 ± 0.038	C	0.004 ± 0.008	0.1	
	2	0.014 ± 0.016	B	0.01 ± 0.01	0.2	
1253−055	1	0.181 ± 0.046	B	0.28 ± 0.01	2.1	
1308+326	1	0.343 ± 0.014	B	0.313 ± 0.002	2.1	
1606+106	3	0.089 ± 0.049	C	0.38 ± 0.03	5.1*	ID
	4	−0.092 ± 0.032	B	0.30 ± 0.02	10.4*	ID
1611+343	2	0.063 ± 0.022	B	0.06 ± 0.04	0.1	
1803+784	4	0.027 ± 0.017	B	−0.01 ± 0.01	1.9	
1921−293	1	0.241 ± 0.110	B	0.19 ± 0.06	0.4	
2136+141	4	0.167 ± 0.044	B	0.02 ± 0.01	3.3*	ID
2145+067	3	0.105 ± 0.036	D	0.03 ± 0.01	2.0	
	4	0.046 ± 0.030	C	0.027 ± 0.003	0.6	
2200+420	1	1.253 ± 0.136	B	1.41 ± 0.13	0.8	
	2	1.288 ± 0.128	C	1.12 ± 0.22	0.7	
	4	1.183 ± 0.146	D	0.99 ± 0.18	0.8	
2230+114	6	0.265 ± 0.130	B	0.03 ± 0.04	1.7	
2234+282	1	0.072 ± 0.031	B	0.12 ± 0.05	0.8	
2243−123	1	0.006 ± 0.060	D	0.11 ± 0.10	0.9	
	2	0.118 ± 0.033	B	0.29 ± 0.03	3.9*	TB

[a] Component identifications and proper motions are from Table 4 of this paper.

[b] Component identifications and proper motions are from Table 2 of K04.

[c] The significance of the difference in the two proper motions was computed from the probability associated with the reduced χ^2 that was computed from the fit of the two proper motions to their weighted average. Entries with asterisks indicate a probability $p < 0.01$ that the two proper motions are independent measurements of the same proper motion.

[d] For the entries with asterisks in the previous column, this column indicates the cause or causes of the different proper motion measurements in the two surveys: MF = the model fits give different measured component positions in the two surveys at similar epochs; TB = measurements on different time baselines have caused different fitted proper motions; ID = different component identification schemes were used by the two surveys. See the text in § 5 for a discussion of each of these.
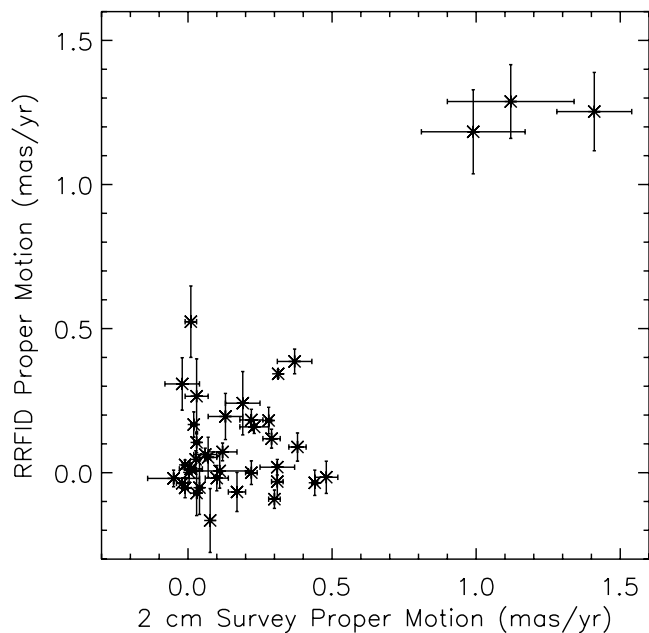
Fig. 9.—Measured proper motion from the RRFID kinematic survey (this paper) vs. the measured proper motion from the 2 cm survey (K04), for the common components listed in Table 6. Some error bars are smaller than the plotting symbols.
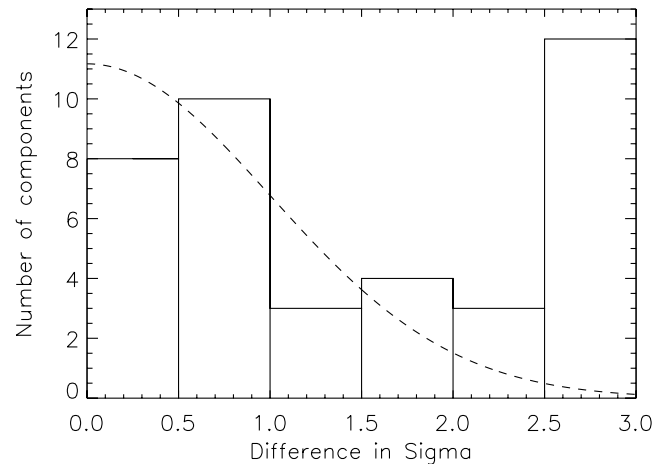

Fig. 10.—Histogram of the difference in σ between the RRFID proper motion measurement and the 2 cm survey proper motion measurement for the 40 common components in Table 6. The 12 components with >2.6 σ difference are all included in the rightmost bin. The dashed line shows the theoretical normal distribution for the remaining 28 components.

components can be identified. For multiepoch VLBI surveys then, the distribution of apparent speeds seems to be a robust and repeatable measurement (witness the statistical agreement between the apparent speed distributions measured by the 2 cm survey and this paper, as discussed in § 4.1), but we would caution against relying too much on the apparent speed measured for a particular source, unless the component identification in that source is well constrained by having many more observed epochs than model components, or by seeing that particular component as a strong, distinct feature on the images.

Whether or not two series of VLBI observations agree on their measurements of component motions is a separate question from whether or not those motions are a realistic portrayal of what is going on in the jet. Comparison of VLBA observations with simulations of relativistic jets by Gomez (2005) led to the conclusion that the interpretation of VLBI images as a series of Gaussian moving components is an overly simplistic idealization of more intricate jet emission patterns. Some of the disagreements on "component" motions discussed above then probably arise from different approximations of an underlying complex flow that cannot be fully resolved. However, because the VLBI data are only partially resolved, models consisting of a series of Gaussians with a few free parameters do fit the observed visibilities with reasonable reduced χ^2 values, so unless the linear resolution of jet observations increases, it will be difficult to constrain fits to the more complex emission patterns suggested by the numerical simulations. Despite these problems, the moving Gaussian approximation does provide some valuable information about the sources. As shown here, the apparent speed measurements in this approximation are repeatable for about 75% of the sources, and correlations between the measured apparent speeds and other source properties (in, for example, the MOJAVE survey [Lister 2006]) have shown that the fastest measured apparent speeds in the Gaussian approximation are a good realization of the bulk apparent speeds of the jets.

6. CONCLUSIONS

Some of the major conclusions from the present work are as follows:

1. The Radio Reference Frame Image Database has been validated as a valuable tool for studying jet kinematics. All 8 GHz VLBA images in the RRFID for all 87 sources observed at three or more epochs over the years 1994–1998 were considered, and in total we identified and measured apparent speeds for 184 jet components in 77 of these sources, with an average of 11 epochs of observation per source. About half of these sources are not present in other large multiepoch VLBI surveys, so these results represent the first information on the jet kinematics in these sources.

2. The measured apparent speed distribution for the 94 best-measured components (Fig. 4) shows a peak at low apparent speeds that is consistent with a population of stationary components, a tail extending out to apparent speeds of about 30c, and a mean apparent speed of 3.6c. The distribution is statistically consistent with the apparent speed distribution found by the radio-selected 2 cm survey, but differs significantly from the apparent speed distribution in gamma-ray blazars measured by Jorstad et al. (2001).

3. For the 36 sources in common between this survey and the 2 cm survey, we made a component-by-component comparison of the measured apparent speeds. Significant disagreements are found in about 25% of the apparent speed measurements, usually due to different assumed component identification schemes. This first large-scale test of the repeatability of apparent speed measurements shows that component identification can be a significant problem that is probably best avoided by short spacings between observing epochs.

Some other results are:

4. There is a difference between the fastest measured apparent speeds in the quasars and BL Lac objects, with the quasar jets being faster, but the significance of this result is a rather low 94%.

5. We checked for accelerated radial motion and nonradial trajectories in the individual component position data. We found significant nonradial motion for six components and report a tentative detection of accelerated radial motion for three components.

6. There was no significant statistical difference in the apparent speed distributions of the EGRET-detected and nondetected sources; however, this survey does not contain a complete gamma-ray or radio-selected sample.

This paper has presented some of the first astrophysical results to be derived from the RRFID, and it is clear that this database can provide scientific results that compare favorably with those of other large VLBI surveys. However, we reiterate that the RRFID is not a complete flux-limited sample and that the exact nature of the biases that this lack of predefined selection criteria may introduce into statistical quantities calculated from the RRFID is not known. This paper has only presented the apparent jet speed measurements made from the first 5 years of the RRFID (1994–1998), with a minimal amount of further analysis. Many more studies are possible with the current set of reduced RRFID data, and some of these will be pursued in future papers. Such studies include a paper in preparation on the misalignment angles between the parsec- and kiloparsec-scale structures in the RRFID sources, and a future study of possible transverse jet structures. Those studies will take advantage of the 2 GHz data present in the RRFID, in addition to the 8 GHz data that were used in this paper, and will not be limited to the sources observed at three or more epochs that we have restricted ourselves to here.

In addition, astrometric and geodetic VLBA observations (the RDV experiment series) have continued at the rate of six epochs per year since the end of the RRFID data included in this paper in 1998 December. We are currently working as part of a collaborative effort to complete the imaging of the 30 RDV experiments observed during the years 1999–2003, which will make the RRFID complete over a 10 yr time baseline, with approximately 50 epochs per source for the best-observed sources. Once the RRFID has been updated with a longer time baseline, we can update the apparent speed measurements given in this paper, significantly reducing the random errors. Those updated apparent speeds can then be used for more detailed studies of jet physics, including studies of correlations with other source properties, radio source evolution and unification, and cosmology. With a long time baseline and dense epoch spacing providing up to 50 observed epochs per source, the continuation of the RRFID kinematic survey will continue to provide a valuable comparison to other active VLBI surveys such as the MOJAVE and MOJAVE-II surveys.

REFERENCES

Agudo, I., Gomez, J.-L., Martí, J.-M., Ibáñez, J.-M., Marscher, A. P., Alberdi, A., Aloy, M.-A., & Hardee, P. E. 2001, ApJ, 549, L183

Blandford, R. D., & Königl, A. 1979, ApJ, 232, 34

Britzen, S., Vermeulen, R. C., Taylor, G. B., Pearson, T. J., Readhead, A. C. S., Wilkinson, P. N., & Browne, I. W. 1999, in ASP Conf. Ser. 159, BL Lac Phenomenon, ed. L. O. Takalo & A. Silanpää (San Francisco: ASP), 431

Cohen, M. H., Cannon, W., Purcell, G. H., Shaffer, D. B., Broderick, J. J., Kellermann, K. I., & Jauncey, D. L. 1971, ApJ, 170, 207

Dermer, C. D. 1995, ApJ, 446, L63

Fey, A. L., & Charlot, P. 1997, ApJS, 111, 95

———. 2000, ApJS, 128, 17

Fey, A. L., Clegg, A. W., & Fomalont, E. B. 1996, ApJS, 105, 299

Fey, A. L., et al. 2004, AJ, 127, 3587

Gomez, J. L. 2005, in ASP Conf. Ser. 340, Future Directions in High Resolution Astronomy, ed. J. D. Romney & M. J. Reid (San Francisco: ASP), 13

Gomez, J. L., Marti, J. M. A., Marscher, A. P., Ibanez, J. M. A., & Marcaide, J. M. 1995, ApJ, 449, L19

Hartman, R. C., et al. 1999, ApJS, 123, 79

Homan, D. C., & Lister, M. L. 2006, AJ, 131, 1262

Homan, D. C., Ojha, R., Wardle, J. F. C., Roberts, D. H., Aller, M. F., Aller, H. D., & Hughes, P. A. 2001, ApJ, 549, 840

Jorstad, S. G., Marscher, A. P., Mattox, J. R., Wehrle, A. E., Bloom, S. D., & Yurchenko, A. V. 2001, ApJS, 134, 181

Kellermann, K. I., Vermeulen, R. C., Zensus, J. A., & Cohen, M. H. 1998, AJ, 115, 1295

Kellermann, K. I., et al. 2004, ApJ, 609, 539 (K04)

Kovalev, Y. Y., et al. 2005, AJ, 130, 2473

Lister, M. L. 1999, Ph.D. thesis, Boston Univ.

———. 2006, in ASP Conf. Ser. 350, Blazar Variability Workshop II: Entering the GLAST Era, ed. H. R. Miller et al. (San Francisco: ASP), 139

Lister, M. L., & Homan, D. C. 2005, AJ, 130, 1389

Mattox, J. R., Hartman, R. C., & Reimer, O. 2001, ApJS, 135, 155

Napier, P. J., Bagri, D. S., Clark, B. G., Rogers, A. E. E., Romney, J. D., Thompson, A. R., & Walker, R. C. 1994, Proc. IEEE, 82, 658

Pearson, T. J. 1995, in ASP Conf. Ser. 82, Very Long Baseline Interferometry and the VLBA, ed. J. A. Zensus, P. J. Diamond, & P. J. Napier (San Francisco: ASP), 268

Pearson, T. J., & Readhead, A. C. S. 1984, ARA&A, 22, 97

Petrov, L., & Ma, C. 2003, J. Geophys. Res. Solid Earth, 108, 2190

Piner, B. G., & Kingham, K. A. 1997a, ApJ, 479, 684

———. 1997b, ApJ, 485, L61

———. 1998, ApJ, 507, 706

Rogers, A. E. E. 1970, Radio Sci., 5, 1239

Sowards-Emmerd, D., Romani, R. W., & Michelson, P. F. 2003, ApJ, 590, 109

Vermeulen, R. C. 1995, Proc. Natl. Acad. Sci., 92, 11385

Vermeulen, R. C., Britzen, S., Taylor, G. B., Pearson, T. J., Readhead, A. C. S., Wilkinson, P. N., & Browne, I. W. A. 2003, in ASP Conf. Ser. 300, Radio Astronomy at the Fringe, ed. J. A. Zensus, M. H. Cohen, & E. Ros (San Francisco: ASP), 43

Vermeulen, R. C., & Cohen, M. H. 1994, ApJ, 430, 467

Véron-Cetty, M.-P., & Véron, P. 2003, A&A, 412, 399

Vlahakis, N., & Königl, A. 2004, ApJ, 605, 656

Whitney, A. R., et al. 1971, Science, 173, 225

Zensus, J. A., Cohen, M. H., & Unwin, S. C. 1995, ApJ, 443, 35

Zensus, J. A., Ros, E., Kellermann, K. I., Cohen, M. H., Vermeulen, R. C., & Kadler, M. 2002, AJ, 124, 662